POLITECNICO DI MILANO

School of Industrial and Information Engineering

Department of Chemistry, Materials and Chemical Engineering

"G. Natta"

Master of Science in Materials Engineering and Nanotechnology

kesterite CZTS films via Cu-Zn-Sn electrodeposition followed by sulfurization

Supervisor: **Prof. Luca Magagnin**

Author **Alaa Khaled Meetkees**

Student no. **882712**

Academic year 2018/2019

List of Tables and Figures

Figure 6.6: X-ray patterns for CZTS films after sulfurization of Cu-Zn-Sn layers at 500 _C as a function of Zn/Sn ratio.

Figure 6.7: a) Top-down SEM image and b) cross section of CZTS film with Zn/Sn ratio 1.34.

Figure 6.8: a) Raman Spectra for CZTS films and corresponding Lorentzian curve fittings for samples with b) Zn/Sn ratio 0.72, c) 1.01 and d) 1.34.

Figure 6.9: a) Photocurrent density vs. potential curves for CZTS films after sulfurization at 500 °C. The inset shows details in a window of more negative voltages and b) Transient photocurrent response of CZTS film at -0.9 V vs. MSE.

Figure 6.11: X-ray patterns of CZTS films sulfurized at 500 °C (Zn/Sn = 1.01) and 550 °C (Zn/Sn = 0.98).

Figure 6.12: Raman Spectroscopy with a) 514 nm excitation wavelength and b) 785 nm for CZTS films sulfurized at 500 °C (Zn/Sn = 1.01) and 550 °C (Zn/Sn = 0.98).

Figure 6.13: Lorentzian fitting for Raman spectra with excitation wavelength 785 nm for CZTS films sulfurized at a) 500 °C (Zn/Sn = 1.01) and b) 550 °C (Zn/Sn = 0.98).

Figure 6.14: Photocurrent-potential curves for CZTS films sulfurized at 500 °C and 550 °C with different Zn/Sn ratio.

Summary

Photovoltaic (PV) solar cells are among the fastest growing alternative energy technologies. The number of commercial installations has witnessed an exponential growth since 1975, reaching a global operating capacity of 177 GW in 2014, and has the potential to generate 10% of the current global power requirement. Unfortunately, the PV market is dominated by relatively high cost Si based solar cells, with a limited share of thin film devices reliant on semiconductor compounds that are toxic like CdTe, or using globally scarce elements such as In in Cu(In,Ga)(S,Se)2 (CIGS). Global expansion of the PV market should benefit from the development of earth abundant, environmentally friendly and low cost semiconductor based solar cells such as kesterite Cu2ZnSnS4 (CZTS) compound. CZTS absorber layer material is attractive for photovoltaic applications due to its strong light absorption and the suitable band gap. CZTS has a band gap similar to commercially available, 21.7% efficiency, CIGS based solar cells; however, the record efficiency of CZTS (Se) based solar cell at present is 12.6%, low if compared to CIGS based solar cell. At the current stage of CZTS development, the lower efficiency of CZTS in comparison with CIGS based solar cells can be essentially traced back to the lower phase purity of the former, due to the facilitated formation of secondary phases. However, the phase purity is not the only cause of reduced efficiency. Another important aspect is disorder in the CZTS layer, where the Cu and Zn cation sites in the Z = 1/4 and Z = 3/4 planes (for the space group I4), also plays a key role. The disorder in the CZTS crystal causes band gap fluctuations which lower the open circuit voltage, hence efficiency. It is therefore important not only to quantify the degree of order in the CZTS layer to better understand material quality, but also to improve knowledge of the growth processes with the aim to develop a production method for CZTS with high phase purity and superior crystal quality. A solution-based hydrazine process followed by selenization/ sulfurization has led to the highest power conversion efficiency, using Cu-poor and Zn-rich CZTSSe material. Electrochemical deposition followed by sulfurization/selenization is also among the most promising synthesis methods, considering its ability to closely control composition, the potential for scale-up, and the high utilization of the raw elements. The current record efficiency for electroplated CZTS

(7.99%) has been obtained by sulfurization of electrodeposited stacked metal layers. Recently, a CZTS layer formed via sulfurization of a ternary alloy grown by pulsed deposition reached 6.28% efficiency, mostly due to the improvement of compositional uniformity. However, even with this two-stage process, it is difficult to obtain phase pure CZTS. The first problem is the loss of elements occurring during the sulfurization process ; in particular, the evaporation of Sn compounds above 230 °C; in some cases however the loss of Zn has also been reported. The second problem is the decomposition of CZTS into binary and ternary compounds during sulfurization and the successive cooling process, particularly at the surface region.

Despite the large body of work available on the compositional control of ternary alloys for CZTS layers, an assessment of the compositional deviation from stoichiometry on the loss of elements and on the formation of secondary phases in CZTS layers for electrodeposited alloys is still missing. The aim of the present work is to achieve a better understanding of the influence of precursor alloy composition and sulfurization temperature on the formation of secondary phases due to elemental losses during sulfurization and cooling. In this work, we grow Cu-Zn-Sn layers and we sulfurize these metallic layers at 500 °C or 550 °C to form the CZTS kesterite phase. The sulfurization temperatures were chosen high enough to induce the transformation of ZnS and Cu2SnS3 into CZTS, but sufficiently low to avoid secondary phases such as SnS2 . We find that slight changes in the precursor alloy composition significantly affect the loss of elements, hence hindering the growth of phase pure CZTS layers. We also observe different compositional shifts for precursor alloys with same initial composition but grown at different electrochemical potentials. X-ray diffraction, Raman Spectra and photocurrent show that, within the compositional range investigated, increasing Zn/Sn ratio improved phase purity, crystal quality and photo- electrochemical response. Sulfurization at 550 °C resulted in zinc loss from the layers, but phase purity and crystal quality were better than those sulfurized at 500 °C. The best photoelectrochemical response, 0.99 mA/cm2 at -0.95 V (vs. MSE), under 1.5AM illumination, was obtained for CZTS layer sulfurized at 550 °C.

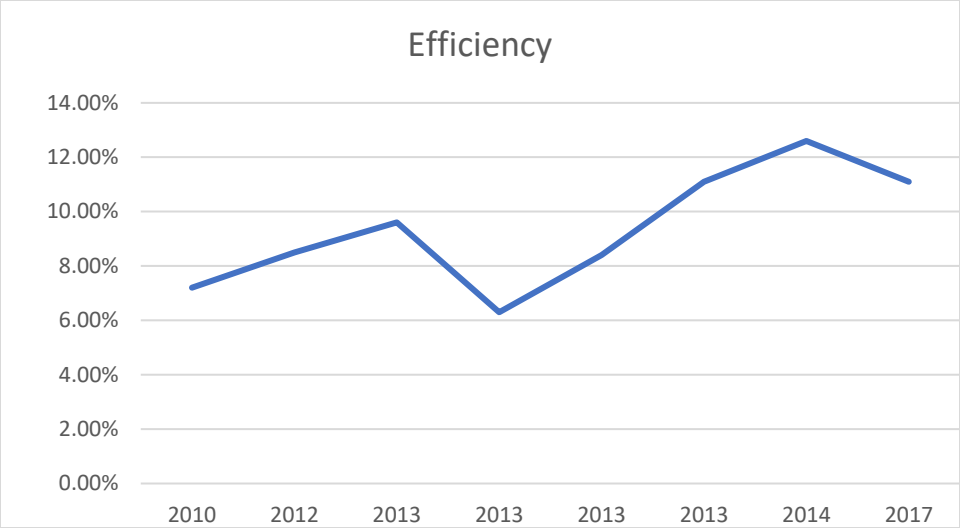

Improvement of conversion efficiency on CZTS-based thin film solar cells.

Sommario

Le celle solari fotovoltaiche (PV) sono tra le tecnologie di energia alternativa con la crescita più rapida. Il numero di installazioni commerciali ha visto una crescita esponenziale dal 1975, raggiungendo una capacità operativa globale di 177 GW nel 2014 e ha il potenziale per generare il 10% dell'attuale fabbisogno energetico globale. Sfortunatamente, il mercato fotovoltaico è dominato da celle solari a base di Si relativamente costose, con una quota limitata di dispositivi a film sottile che dipendono da composti semiconduttori tossici come CdTe o che utilizzano elementi scarsi a livello globale come In in Cu (In, Ga) (S, Se) 2 (CIGS). L'espansione globale del mercato fotovoltaico dovrebbe beneficiare dello sviluppo di celle solari a base di semiconduttori a basso costo, ecocompatibili come il composto di kesterite Cu2ZnSnS4 (CZTS). Il materiale dello strato assorbitore CZTS è attraente per le applicazioni fotovoltaiche grazie al suo forte assorbimento della luce e all'adeguato gap di banda. CZTS ha un gap di banda simile a quello disponibile in commercio, efficienza del 21,7%, celle solari basate su CIGS; tuttavia, l'efficienza record delle celle solari basate su CZTS (Se) al momento è del 12,6%, bassa se confrontata con le celle solari basate su CIGS. Nella fase attuale dello sviluppo CZTS, la minore efficienza di CZTS rispetto alle celle solari basate su CIGS può essere essenzialmente ricondotta alla purezza di fase inferiore della prima, a causa della formazione facilitata di fasi secondarie. Tuttavia, la purezza di fase non è l'unica causa di efficienza ridotta. Un altro aspetto importante è il disordine nello strato CZTS, dove anche i siti dei cationi Cu e Zn nei piani Z = 1/4 e Z = 3/4 (per il gruppo spaziale I4) svolgono un ruolo chiave. Il disordine nel cristallo CZTS provoca fluttuazioni del gap di banda che abbassano la tensione del circuito aperto, quindi l'efficienza. È quindi importante non solo quantificare il grado di ordine nello strato CZTS per comprendere meglio la qualità dei materiali, ma anche migliorare la conoscenza dei processi di crescita con l'obiettivo di sviluppare un metodo di produzione per CZTS con elevata purezza di fase e qualità dei cristalli superiore. Un processo a base di soluzione di idrazina seguito da selenizzazione / solforizzazione ha portato alla massima efficienza di conversione di potenza, utilizzando materiale CZTSSe povero di rame e ricco di zinco. La deposizione elettrochimica seguita dalla solforizzazione / selenizzazione è anche tra i metodi di

sintesi più promettenti, considerando la sua capacità di controllare da vicino la composizione, il potenziale di ingrandimento e l'elevato utilizzo degli elementi grezzi. L'attuale record di efficienza per CZTS elettrodeposto (7,99%) è stato ottenuto mediante solforazione di strati metallici sovrapposti elettrodepositi. Recentemente, uno strato CZTS formato mediante solforazione di una lega ternaria cresciuta per deposizione pulsata ha raggiunto un'efficienza del 6,28%, principalmente a causa del miglioramento dell'uniformità compositiva. Tuttavia, anche con questo processo in due fasi, è difficile ottenere la fase pura CZTS. Il primo problema è la perdita di elementi che si verificano durante il processo di solforizzazione; in particolare l'evaporazione di composti Sn superiori a 230 ° C; in alcuni casi, tuttavia, è stata osservata anche la perdita di Zn. Il secondo problema è la decomposizione di CZTS in composti binari e ternari durante la solforizzazione e il successivo processo di raffreddamento, in particolare nella regione superficiale.

Nonostante l'ampia mole di lavoro disponibile sul controllo compositivo delle leghe ternarie per gli strati CZTS, manca ancora una valutazione della deviazione compositiva dalla stechiometria sulla perdita di elementi e sulla formazione di fasi secondarie negli strati CZTS per le leghe elettrodeposite. Lo scopo del presente lavoro è quello di ottenere una migliore comprensione dell'influenza della composizione della lega precursore e della temperatura di solforazione sulla formazione di fasi secondarie dovute a perdite elementari durante la solforizzazione e il raffreddamento. In questo lavoro, coltiviamo strati Cu-Zn-Sn e solforizziamo questi strati metallici a 500 ° C o 550 ° C per formare la fase della kesterite CZTS. Le temperature di solforazione sono state scelte abbastanza alte da indurre la trasformazione di ZnS e Cu2SnS3 in CZTS, ma sufficientemente basse da evitare fasi secondarie come SnS2. Scopriamo che lievi variazioni nella composizione della lega precursore influenzano significativamente la perdita di elementi, ostacolando quindi la crescita degli strati di fase pura CZTS. Osserviamo anche diversi spostamenti compositivi per leghe precursori con la stessa composizione iniziale ma cresciute con diversi potenziali elettrochimici. La diffrazione di raggi X, Raman Spectra e fotocorrente mostrano che, all'interno della gamma compositiva studiata, l'aumento del rapporto Zn / Sn ha migliorato la purezza di fase, la qualità dei cristalli e la risposta fotoelettrochimica. La solforazione a 550 ° C ha comportato una perdita di zinco dagli strati, ma la purezza della fase e

la qualità dei cristalli erano migliori di quelle solforate a 500 ° C. La migliore risposta fotoelettrochimica, 0,99 mA / cm2 a -0,95 V (contro MSE), con illuminazione a 1,5 AM, è stata ottenuta per lo strato CZTS solforato a 550 ° C.

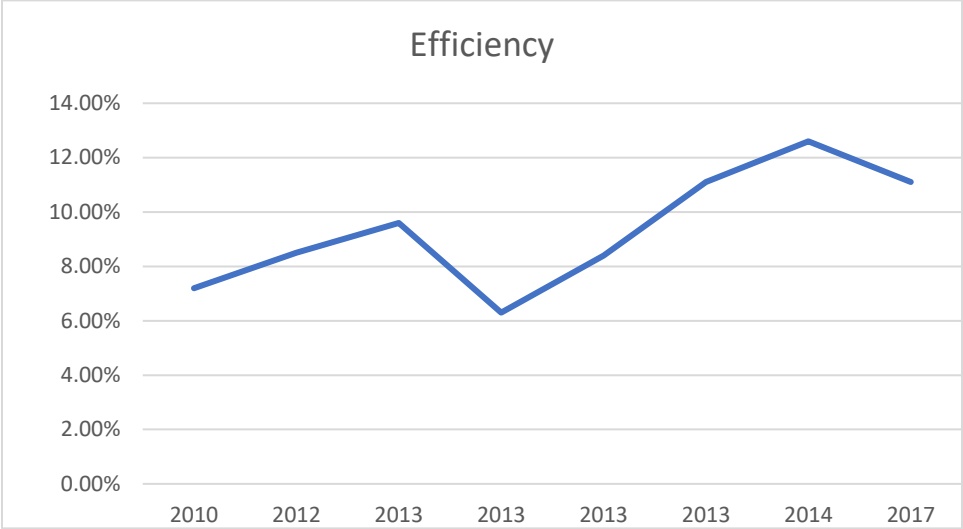

Miglioramento dell'efficienza di conversione su celle solari a film sottile basate su CZTS.

Aim of this work

In both absorber materials a large number of possible intrinsic defects can be formed. The role of intrinsic point defects in CIGS and CZTS is of special importance as they control the recombination losses and hence the performance of the solar cell device. Recombination via (deep-level) defects will limit the conversion efficiency by reduction of open-circuit voltage. Furthermore, intrinsic defects determine the conductivity type of the absorber. Understanding the defect structure in these absorber materials is crucial for further improvement of the cell efficiency. Despite the amount of research already performed on CZTS and CIGS alloys, their optoelectronic properties, defect chemistry and recombination mechanisms are still rather poorly understood.

Theoretical calculations did, so far, not come to an agreement. On the other hand, numerous experiments have been performed with different techniques (photoluminescence (PL), Hall measurements, deep level transient spectroscopy (DLTS), admittance spectroscopy (AS)) on different absorbers (Cu rich/poor, varying stoichiometry) made by a variety of growing techniques (single crystal, epitaxial film, polycrystalline film). As it is therefore difficult to make comparisons, contradictory assignments and long debates concerning interpretations still exist.

A definitive picture of the defect structure is not yet achieved. The aim of this dissertation is the characterization of the defect physics in these absorber materials by means of electric and optical spectroscopy complemented with morphology information obtained by scanning electron microscopy (SEM) and composition information obtained by different analytical methods such as energy-dispersive X-ray spectroscopy (EDX), secondary ion mass spectroscopy (SIMS) and time-of-flight mass spectroscopy (TOFMS).

CHAPTER I: INTRODUCTION to SOLAR ENERGY

1.1 The energy challenge

We live in an exceptional time: the fossil-fuel (coal, oil, natural gas) era. The exploitation of fossil fuel energy distinguishes modern industrial society from all previous eras. Currently over 80% of the energy used by mankind comes from fossil fuels as shown in figure 1.1 which represents the contributions of different energy sources to the world's total energy consumption in 2013.

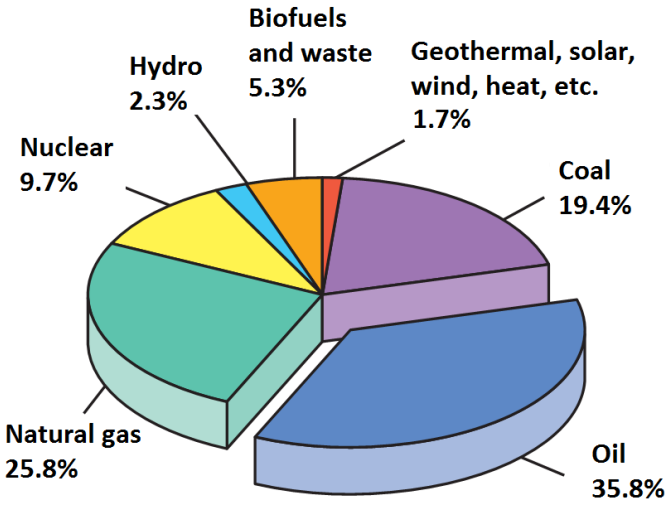

Figure 1.1: World total primary energy supply (2013). Data from the international energy agency (www.iea.org).

The fossil fuel era is an era of easy and cheap energy. Easy because oil, natural gas and coal are much easier to extract and transport than wood, the dominant fuel in the pre-industrial revolution era. Oil provides a unique fuel for transportation and natural gas is ideal for domestic heating and cooking. Furthermore, fossil fuel can easily be stored and has a big role in flexible, quick-start electricity generation. Therefore, it can meet the fluctuation in energy demand. Harnessing coal, oil and gas has led on the other hand to a dramatic expansion in energy use

which entails severe consequences. The drawbacks and problems are listed underneath.

• *Non-renewable* Fossil fuels are a non-renewable resource that is going to exhaust. In the last 140 years we have consumed 120 trillion litres of oil. Currently the world's growing thirst for energy amounts to almost 120 000 litres of oil, 93 000 cubic meters of natural gas, and 221 tons of coal per second. The finite resources of fossil fuels combined with the increasing energy demand will lead to a serious problem.

Due to medical advances and massive increase in agricultural productivity, there has been a rapid population growth. In 1950 the world population was 2.6 billion people, hundred years later in 2050 it is expected that the population will be 9.2 billion people. This overpopulation will result in a huge increase in energy demand. The second reason why energy consumption increases is development. The majority of people living on the earth, lives in countries that are still developing and the increase of the standard of living will ask for more energy to develop the agricultural, industrial, and trading activities. The increase in the world population and the increase of the standard of living in developing countries will lead to an increase of global energy consumption by about 2% per year. The energy consumption will have multiplied by 7 by the year 2100. As fossil fuels are a finite resource this is clearly unsustainable. Alternative energy sources should be used.

• *Global warming and health problems* The use of fossil fuels causes severe damage to human health and the environment. An increase in carbon dioxide concentration leads to an increase in the greenhouse effect that, in turn, increases the average global temperatures and can lead to a climate change. This will impact food security, water availability, fish production, global forests and permafrost melting. Figure 1.2 shows measurements of the CO2 concentration in the air from the year 1000 up to the present. The year 1769 in which James Watt invented the steam engine, which started the industrial revolution, is indicated.

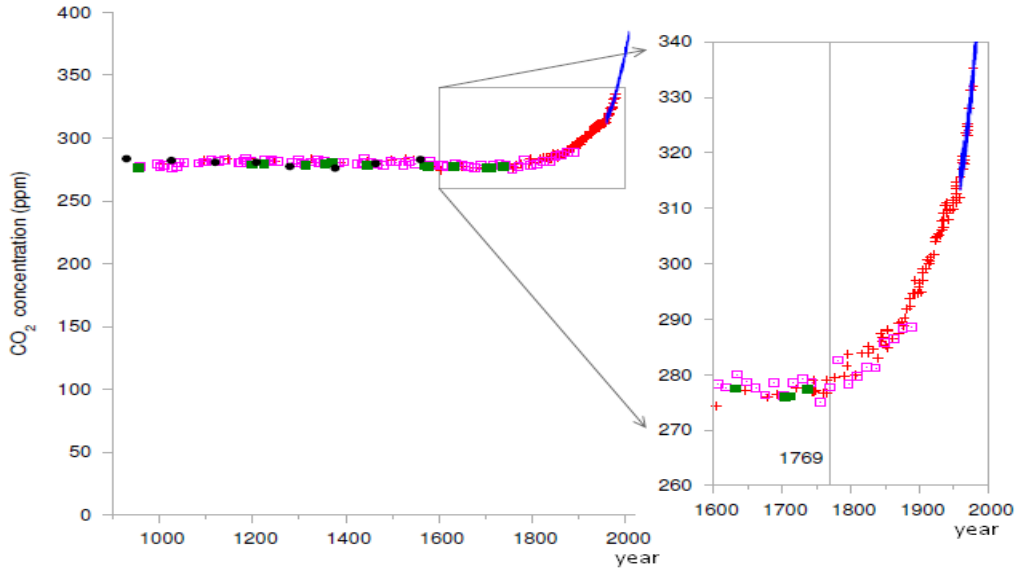

Figure 1.2: Carbon dioxide (CO_2) emission over the last 1100 years

• *Uneven consumption/waste* Another critical aspect concerning fossil fuels is that their uneven allocation, coupled with the uneven waste generation and unfair distribution of wealth, leads to strong disparities in the quality of life among Earth's habitants. As an average, an American consumes about 300 GJ of energy per year, a quantity approximately equal to that consumed by 2 Europeans, 4 Chinese, 17 Indians and 240 Ethiopians. This situation is not preservable.

• *Security and safety* An important point is the security and safety of energy supply. Even if fossil fuels (e.g. oil and natural gas) are still available somewhere in the world, it would be better to rely on an independent energy production. Figure 1.3 shows the energy production and energy consumption for different regions of the world. Some regions do not produce enough for their own needs and must import their energy. In the figure Russia is included in Europe. Russia has large energy resources, including a lot of natural gas. This brings Europe's production and consumption close to each other but does not reflect the real political situation. Indeed, the remaining part of Europe imports a lot of energy from Russia and elsewhere. Europe's dependence on external sources for its oil and gas is already large and is expected to increase the next decade.

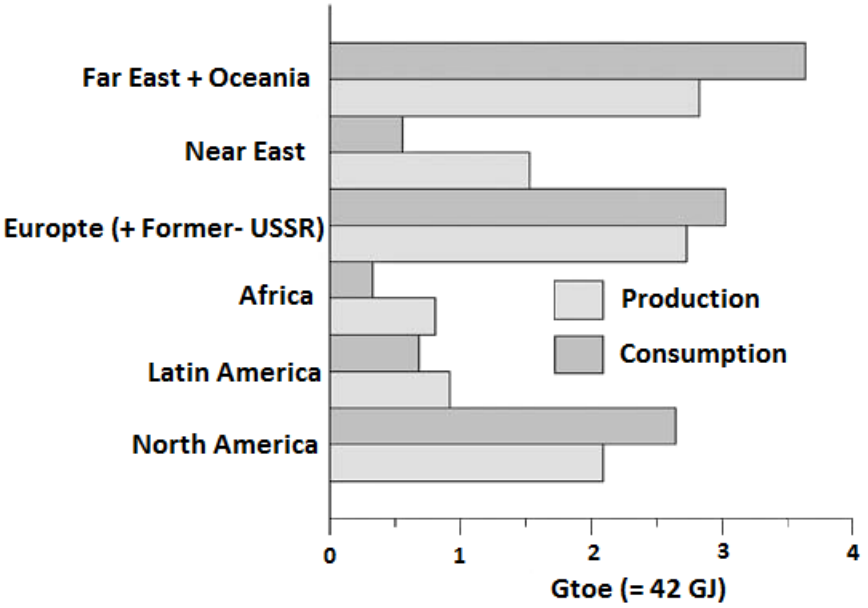

Figure 1.3: Production and consumption of primary energy (energy which has not been subjected to any conversion or transformation process) in different regions of the world, 2006

Concerning safety on the other hand, nuclear fission has serious issues. The energy obtained by nuclear fission does not emit greenhouse gases but it produces radioactive waste, whose safe disposal is an essentially unsolved issue. Other fears are exposure of radioactive materials in nuclear accident or terrorist attacks.

1.2 The huge potential of solar energy

The radiation reaching the surface of the earth is on average (including diffuse and direct light, average over winter/ summer, day/night) 197 W/m2. This received energy amount annually is more than 10 000 times larger than consumed annually by mankind. Solar energy is not only inexhaustible on any conceivable time-scale for human civilization, but is also widely abundant even in a scenario of doubling or tripling current energy demand. Presently, the solar energy incident on only about 5% of the desert area of the earth would be sufficient to satisfy the entire need for electric power in the world. Storage and transport of electricity is of course another issue. Many technologies are used to exploit solar radiation. With properly designed technologies the solar electromagnetic flux can be converted into heat, electricity and biofuels which are the three essential forms of energy used in everyday life.

1.3 Photovoltaics

Photovoltaics (PV) includes the direct conversion of sunlight into electric energy. The transformation relies on the photovoltaic effect: an electron-hole pair, which is created after a semiconductor is exposed to light, is separated where after the free carriers are collected. A direct current is produced, which can be converted to an alternating current with electronic devices.

1.3.1 Advantages-disadvantages

PV has many benefits: highly reliable, renewable, pollution-free, noise free, low in operation costs (no moving parts) and construction costs, operating over a quite long period of time (in the case of grid applications photovoltaic modules can last more than 30 years). Electricity can be produced on demand at the place of consumption, avoiding transport losses over large distances. It needs no exploration for new sunshine reservoirs and no wars to get access over its fuel.

It can be constructed to any size based on energy requirements. Besides these advantages there are also some drawbacks. Although no greenhouse gas is emitted during operation of a photovoltaic cell, this is currently not the case for its fabrication. Solar cell technology requires a lot of energy, the initial cost (labor, materials, energy, . . .) is quite high.

The energy payback time (how long a PV system must operate to recover the energy consumed to produce it) is critical to technology viability. Thin-film technologies, which are studied in this work, perform on the module level better by at least a factor of two, less than one year, then the current dominant technology with multi crystalline Si modules (2-3 years) in southern regions [35]. Systems deployed in the next generation are expected to have shorter payback times.

Another concern is that a PV system does not generate power when the sun does not shine. Supplemental means of energy storage are required. This also holds when the consumer is not connected to the electric grid. In ‘stand-alone’ applications batteries may be required to store electricity for use in periods without sunlight.

1.3.2 History

The photovoltaic effect was first reported by Edmund Bequerel in 1839 when he observed that the action of light on a silver coated platinum electrode, immersed in electrolyte, produced an electric current. Willoughby Smith (1873) reported about the photoconductivity of selenium. In 1876 William Adams and Richard Day discovered the photovoltaic effect in selenium which was contacted by two heated platinum contacts and exposed to light. The first functional solid state photovoltaic cell was made by Charles Fritts in 1883. He coated the semiconductor material selenium with an extremely thin layer of gold as a top contact. He noted, 'the current, if not wanted immediately, can be either stored where produced, in storage batteries or transmitted over a distance and there used. The first intentionally made PV device was a fact.

The early thin-film solar cells were Schottky barrier devices. A semitransparent layer of metal was deposited on top of the semiconductor. As the current produced was proportional to the intensity of the incident light, the photoconductive materials were used as photographic light meters. The photovoltaic effect in barrier structures was an added benefit, because the light meter could operate without a power supply. During the 1930s Walter Schottky, Neville Mott and others developed the theory of metal-semiconductor barrier layers.

In 1954 researchers at Bell Labs in the USA discovered accidentally that pn-junction diodes generated a voltage when the room lights were on. pn-junctions in silicon were developed by exposing n-type silicon to the boron tricholoride gas so that a p-type upper layer was formed. Within a year, a 6% efficient Si pn-junction solar cell was produced. Because the production cost was estimated very high, the cells were not considered for power generation for several decades. During the 1950s and 60s, silicon solar cells were widely developed for applications in space. Also in 1954 results of a thin-film heterojunction solar cell based on Cu2S/CdS having 6% efficiency were published. In the following years studies on GaAs, InP and CdTe were performed.

These studies were stimulated by theoretical work of Shockley and Queisser which developed the fundamental theory of a pn-junction solar cell. In 1973 most governments began programs to encourage renewable energy after the first World Oil Embargo. The energy crisis experienced

by the oil-dependent western world gave an urgency to research (with increasing funding) and application of alternative sources.

In the 1980s companies attempted to scale up the thin-film PV technologies like a-Si and CuInSe2. These cells achieved efficiencies larger than 10% for small area (1 cm2) devices which were made with carefully controlled laboratory scale equipment. The scale up was far more complicated than just scaling the size of the equipment. The first consumer-sized, small-scale power applications were developed. The solar-powered calculator pioneered by Japanese electronics companies is the best-known example. During the 1990s the economics of photovoltaics improved primarily through economies of scale. The costs for PV modules had fallen but once again there was a lack of financial and technical resources for development of inverters and sun trackers, which had only limited application outside of a PV power system. Further during this period an attempt to help developing countries by rural electrification of remote villages was made. Late in the 1990s PV cells were integrated into standard building products, such as windows or roofs, lowering the incremental cost of PV installation.

1.3.3 Global PV capacity

By the end of 2013, the installed photovoltaic capacity reached 139 gigawatts (GW) on the planet. Photovoltaics grew fastest in China, followed by Japan and the United States, while Germany remains the world's largest overall producer of photovoltaic power with a total capacity of 35.5 GW, contributing almost 6% to its national electricity demands.

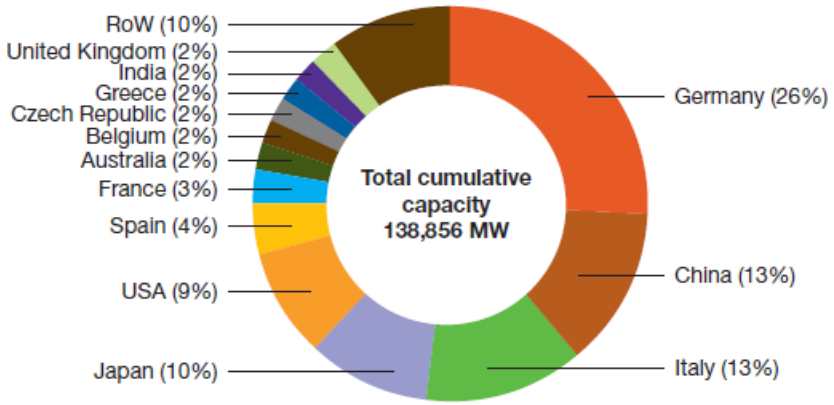

Figure 1.4: Global PV cumulative installed capacity share (2013).

By 2018 the worldwide photovoltaic capacity is projected to have doubled (low scenario of 320 GW) or even tripled (high scenario of 430 GW). The European Photovoltaic Industry Association (EPIA) expects the fastest PV growth to continue in China, South-East Asia, Latin America, the Middle-East, North Africa, and India.

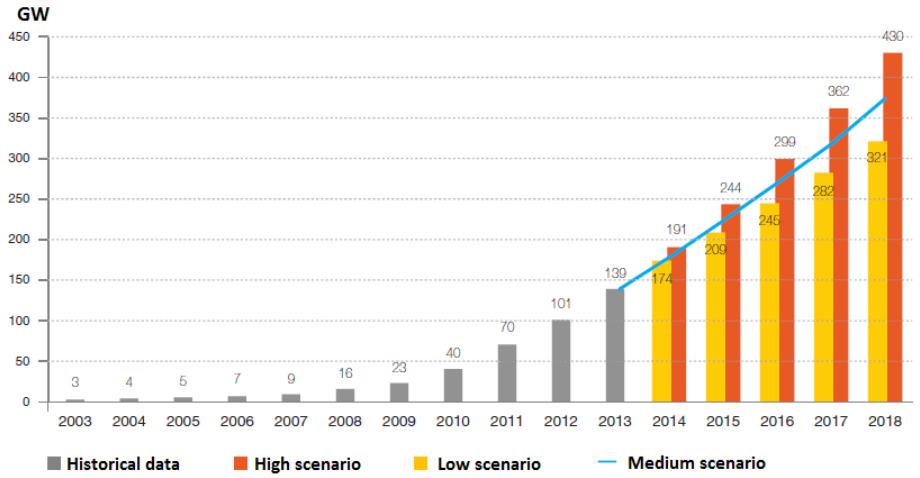

Figure 1.5: Global PV cumulative scenario until 2018.

1.3.4 From thick to thin solar cell absorbers

The photovoltaic market today is mostly dependent on single crystalline and polycrystalline silicon solar cells. In 2013 Si technologies still made up almost 90% of the world PV market as shown in figure 1.6. This dominance decreases with the growth of the thin-film industry

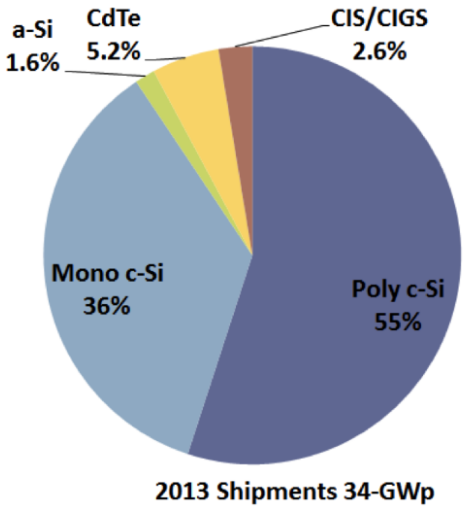

Figure 1.6: Market share by technology in 2013 (www.renewableenergyworld.com).

As Si is an important material for the electronics industry, a lot more information is available

about the physical, chemical and optical properties of this semiconductor than for any other material. For monocrystalline silicon, the maximum recorded cell efficiency reaches 25.6% (Panasonic) in the laboratory and 20.4% (test centre: FhG-ISE) for polycrystalline cells.
In a commercial application, the typical efficiency of a module is 18.5% for multi crystalline Si (Q-Cells) and thus well below that obtained in laboratory conditions.
Si has relatively small absorption coefficient related with its indirect band gap (103 cm−1 around 1.5 eV). Therefore, a thick Si wafer of around 250 _m is used to have sufficient absorption of light. The fabrication of the Si wafers (50% of the cost on module level), encapsulation and wiring requires a lot of energy which results in a high cost. The latter is also related to the high temperature (above 1400_C) which is needed to obtain pure Si from sand after several melting steps.
A goal for the future is to produce solar cells with lower payback time. This can be done by making thin-film photovoltaic cells which needs less material and less energy for processing (temperature for processing < 550_C). The technology makes efficient use of raw materials: while 0.5-1 kg/m2 of semiconductor grade silicon is required for a conventional module, the material consumption per square meter for the active films of a CuInSe2 module is: 7-20 g molybdenum,1.5-4 g copper, 3-9 g indium, 7-20 g selenium, and 1-3 g zinc (depending on the exact module structure and yield). This implies that the total material input is comparable to the material used for just the grid metallization of silicon modules. Another advantage of the thin-film solar cells is that they are light weight (due to the thin absorber layer and the possibility to use polymer substrates) which is attractive to space industry. The cost can be further reduced by roll-to-roll processing and the use of low cost substrates such as glass sheet, metal or polymer foil. The use of flexible substrates can moreover broaden the range of applications.
The main characteristics of the semiconductor absorber materials for thin-film solar cells are direct band gaps and high absorption coefficients. Different semiconductors meet these criteria:
amorphous silicon, cadmium telluride (CdTe), copper indium galium diselenide (Cu(In1-xGax)Se2, CIGS) and copper zinc tin sulfide (Cu2ZnSnS4, CZTS). The main characteristics for each

of this thin-film semiconductor absorber type are listed underneath. The research in this thesis focusses on CIGS and CZTS thin-film solar cells.

- **Hydrogenated amorphous silicon** (a-Si:H), which has assigned a direct band gap (Eg = 1.6-1.8 eV), has a high absorption coefficient (_ = 104-105/cm) [36] in the visible range of the solar spectrum. A 1 _m thick a-Si:H layer is sufficient to absorb 90% of the solar energy with energy larger than the band gap. The efficiency of amorphous silicon thin-films (13%) is much smaller than those of crystalline Si cells. The light induced degradation of the modules is a great issue.
- **CdTe** has a nearly optimally match to the solar spectrum for photovoltaic energy conversion

(Eg = 1.5 eV, _ > 104/cm for E > 1.5 eV). A record efficiency in lab conditions of 21.0% has been reached (First Solar). The most serious concern about CdTe technology is that Cd and Te are toxic. Cd waste and recycling the modules after their end of life could be hazardous to the environment. This technology is also hindered by the instability of the cells due to contact oxidation, contact degradation and humidity.

- **Cu(In1-xGax)Se**2 (CIGS) is a very promising material for a thin-film solar cell (for Eg _ 1.15 eV > 104/cm for E > 1.2 eV)). Some concerns about CIGS thin-film technology are the complexity of the material (problem for manufacturing) and the use of toxic CdS as buffer layer. Many CIGS related issues (Cu-poor surface layer, role of Na, role of Ga gradient, . . .) are still unresolved. At the moment the lab record efficiency of CIGS on glass is 21.7% (ZSW), 20.4% (Empa) on flexible substrates and 16.6% (Avancis) for a 30 cm·30 cm module.

As there are some restriction on the usage of heavy metals such as cadmium, the limitation in supplies and fluctuation of prices for indium and tellurium, a low-cost, earth abundant alternative with high absorption coefficient and decent band gap was sought and found namely **Cu**2**ZnSn(S,Se)**4 (CZTS) (Eg _ 1.5 eV, _ = 104/cm for E >1.5 eV). The cost of raw material for CZTS PV technology is around 5 and 20 times lower than for CIGS and CdTe respectively. In 1996 a conversion efficiency of 0.66 % was reported a CZTS. Due to research and further development a conversion efficiency of

9.2% (Solar Frontier) for pure sulfide CZTS and 12.6% (IBM) for CZTSSe solar cells has been reached so far.

1.3.5 Efficiency evolution

In figure 1.7 the evolution of the cell efficiencies are provided within different families of semiconductor.

Next to the crystalline (e.g. Si, GaAs) and polycrystalline (e.g. CdTe, CIGS) solar cells, new PV technologies such as organic, dye-sensitized or perovskite solar cells arise and are further developed. The most recent world record efficiency for each technology is highlighted on the right edge of the figure

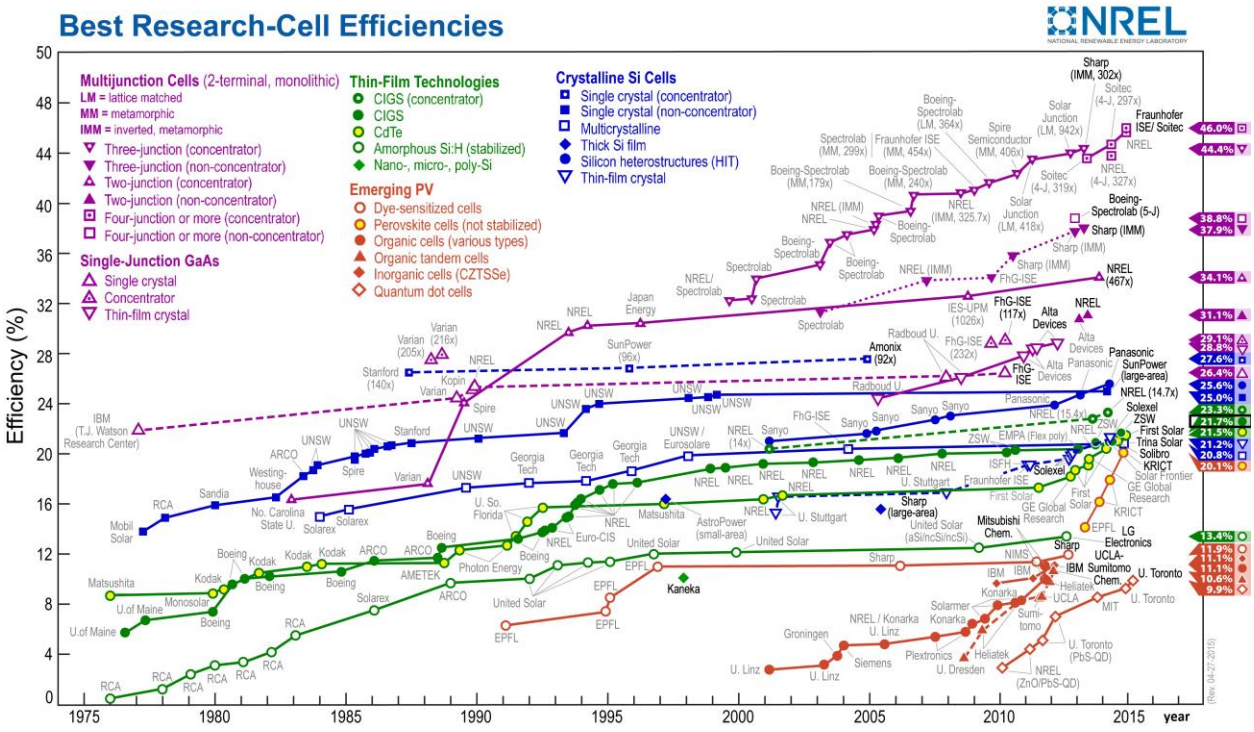

Figure 1.7: Evolution of the best small area solar cell efficiencies PV technologies (27/4/2015).

1.3.6 Manufacturing

A more detailed description of some companies can be found in reference. All of these companies (besides Solibro) were founded at the end of the last century. However the first CIGS modules commercially available in modest volume arrived on the market only over the past few years. Large commercialization of CIGS modules on flexible substrates is in a rather early phase as tools

for roll-to-roll deposition and appropriate equipment are nowadays lacking. In addition for the flexible modules, low-cost flexible encapsulation materials with sufficient moisture blocking properties need to be developed to guarantee long-term stability. A potential future challenge to move CIGS manufacturing to the multi-gigawatt level, needed to develop solar photovoltaic electricity generation into a major electricity source, is related to the abundance of In and Ga. At present there exists an ongoing discussion about whether indium and gallium are abundant enough at affordable prices.

CZTS No solar cell company is using kesterites in their manufacturing process so far. A collaboration between IBM, DelSolar, and Solar Frontier is set in 2010 to develop the CZTS technology further. As kesterite solar cells are (relative to other solar cell technologies) still in their early development stage, more research and development is necessary before manufacturing to compete with technologies already in commercial production. Price has to be low, efficiency has to be high and deposition processes should be made applicable for large scale production.

CHAPTER II

2-CZTS

2.1Structure and composition

CZTS (I2-II-IV-VI4) structure is derived from the chalcopyrite structure CuInS2 by replacing of the In atoms with Sn and Zn. Unlike CIGS wherein the [In]/[Ga] ratio can be varied continuously, the [Zn]/[Sn] ratio in CZTS is far less flexible. The variable for CZTS, which can alter the band gap, is the [S]/[Se] ratio.

The two principal structures of low symmetry are the tetragonal stannite and the kesterite structures (figure 2.1). The difference between these structures lies in the arrangement of the Cu and Zn atoms. The kesterite structure has the lowest energy, but as the bindings energy difference (1.3-3.4 meV/atom) is very small, it is very likely that stannite coexists with kesterite. Furthermore if the Cu and Zn atoms are arranged randomly on their lattice plane, the structure is labelled as partially disordered (PD-kesterite). The disorder among the Cu and Zn cations could be a possible cause of the limited open circuit voltage (and low efficiencies as a consequence). Even 70% ordering in kesterite corresponds to large numbers of Cu/Zn antisite defects. These defects are calculated to cause band gap fluctuations (around 100 meV) which could explain the voltage deficit.

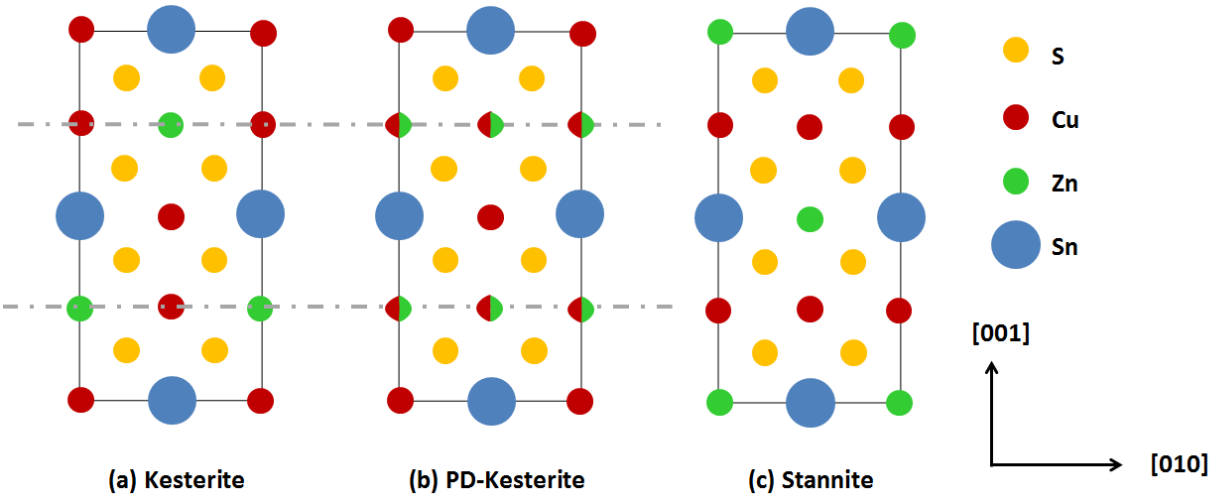

Figure 2.1 Crystal structures of CZTS. Dashed lines indicate the planes of Cu-Zn disorder for kesterite.

The difference between the stannite and kesterite structure is difficult to detect. Because Cu+ and Zn2+ are isoelectronic, X-ray diffraction cannot distinguish between kesterite and stannite. Neutron powder diffraction measurements showed experimentally that the partially disordered kesterite structure can exist. Neutron diffraction is however unsuitable for thin-films as large sample volume is necessary for the analysis. Another method to detect different phases in the material is by Raman spectroscopy. This technique is an optical, non-destructive, surface-sensitive technique which gains information about the phonon behavior of the crystal lattice by detecting frequency shifts of the in-elastically scattered light from the near surface of the sample. As the shifts are specific for each phase, the Raman shifts provide information about the different phases in the material. Reference showed that Raman spectroscopy is convenient tool to track Cu/Zn disorder in CZTS thin-films. A comparison between CZTS powders which differed in the cooling rate after synthesis and thin-films with different post annealing was performed. The determination of the critical temperature for the transition from ordered to disordered kesterite was determined to be relatively low (around 260C). This low critical temperature has important consequences. As CZTS is normally grown at 450-550_C, which is far above the critical temperature, it implies that ordered kesterite cannot exist. Disordered kesterite is formed at these high deposition temperatures. The ordering among Cu and Zn begins only when the temperature drops below 260_C, i.e. during post-synthesis cooling. The low temperature final step of the cooling seems to determine the level of disorder and hence the CuZn and ZnCu defect concentrations which are decisive for the device characteristics. Details on the low temperature part of the cooling wherein the ordering apparently occurs

2.2 Secondary phases

The comparatively low efficiencies of CZTS thin-film solar cells are ascribed to inhomogeneitiesdue to secondary phases. Therefore, secondary phases should be a avoided during crystal growth. It is however very challenging to grow pure CZTS as the single-phase

region of CZTS in the phase diagram is very narrow (figure 2.2). The formation of secondary phases such as ZnS, SnS, CuS, Cu2S, CuxSnSy (CTS) is very likely. Both CuS and CTS phases have small band gaps that can cause shunting and can act as detrimental recombination centres. ZnS, on the other hand, is a highly resistive, wide band gap semiconductor with less negative impact on efficiency.

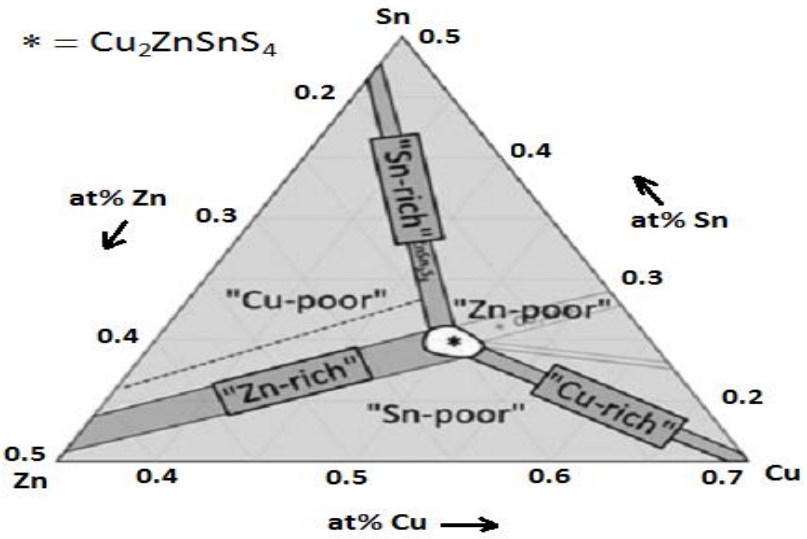

Figure 2.2 The pseudo-ternary phase diagram of the Cu_2S-ZnS-SnS_2 system at 400_C in which a stoichiometric amount of S is assumed

So far CZTS solar cells with high performance are slightly Zn-rich and Cu-poor. Under these growth conditions ZnS is the main competing phase. The content control of Zn should be taken very carefully. To avoid the ZnS secondary phase formation, the Zn concentration should not be too high. On the other hand, the Zn concentration should not be too low as large amount of CuZn antisite defects can than be formed.

For increasing solar cell efficiency, the detection and characterization of these secondary phases is important. Nevertheless, it is commonly recognized that detecting secondary phases using only XRD (X-ray diffraction) in CZTS is not as easy as in CIGS.

XRD can usually assign a phase with confidence, unless there are several coexisting phases with similar symmetry and lattice parameters. Unfortunately, this is the case here: kesterite CZTS shares multiple peaks with cubic ZnS and CTS. Furthermore, the small volume of the material renders the measurements difficult. Raman spectroscopy is therefore often combined with XRD results to characterize the phases in a CZTS thin-films. Unfortunately, overlapping peaks also hinder the interpretation of the Raman spectroscopy results.

2.3Absorption

It is commonly recognized that CZTS has an absorption coefficient of 104 cm−1 for photon energies exceeding 1.5 eV. Theoretical studies of the absorption coefficient of CZTS confirm the value of 104 cm−1 at low energy. However at high energies (E > 2.5 eV) the theoretically determined absorption coefficient is higher (about 105 cm−1) compared to experimental studies.

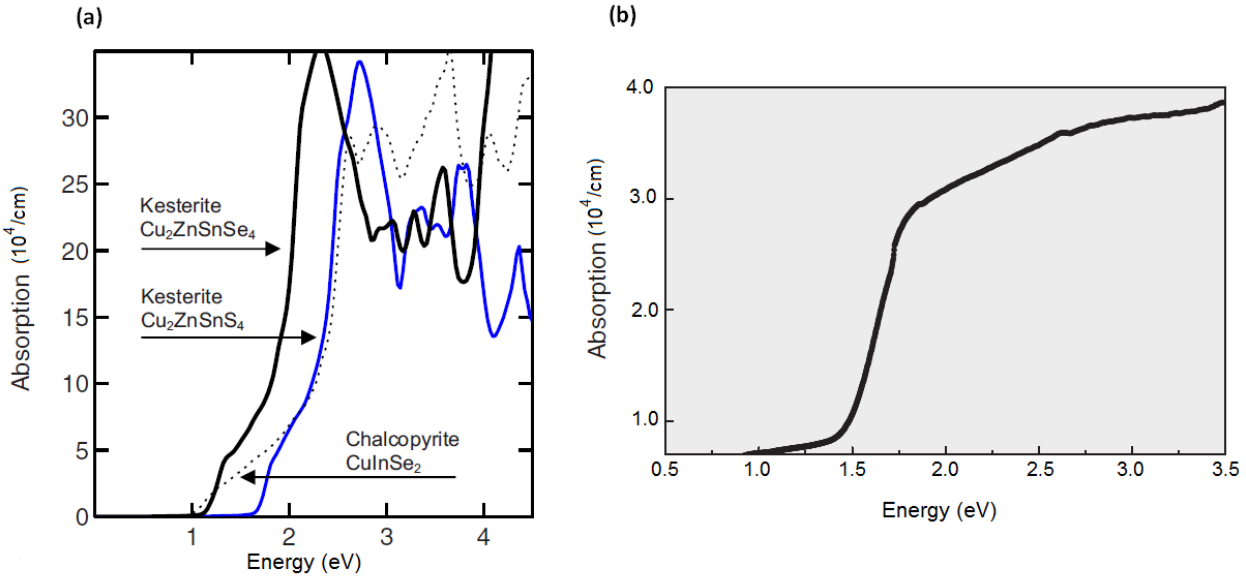

Figure 2.3 Absorption of CZTS (a) theoretical calculation, (b) experimental

2.4 Band gap

The band gap can be varied by changing the [S]/[Se] ratio. In most experiments a band gap of 0.96 eV for Cu2ZnSnSe4 is found, while a band gap close to 1.50 ± 0.01 eV is found

for Cu2ZnSnS4. There are discrepancies on the reported experimentally determined band gap values which can be due to different deposition methods (compositional changes or variations in heat treatments) or to the existence of secondary phases with quite divergent band gap values. In reference the estimated band gap for tetragonal Cu2SnS3 is 1.35 eV (in accordance with), for cubic Cu2SnS3 Eg _ 0.96 eV and for orthorhombic Cu3SnS4 Eg _ 1.60 eV. Cu2-xS has a band gap varying from 1.3 to 2.3 eV. The band gap of ZnS is 3.7 eV. For SnS the direct band gap was determined at about 1.3 eV. Bulk MoS2 has an indirect band gap of 1.15-1.30 eV while a monolayer has a direct band gap (1.8-1.9 eV). Theoretical calculations show that the band gap of the kesterite structure agrees quite well with the experimentally determined band gap (see table 2.4). The band gap value for the disordered kesterite is calculated to be 40 meV lower than for the ordered kesterite structure. For stannite the calculated band gap value is around 150 meV (see table 2.4) lower than for the ordered kesterite structure.

E_g (eV) Stannite	E_g (eV) Kesterite	Difference (eV)
1.38	1.50	0.12
1.42	1.56	0.14
1.30	1.49	0.19

Table 2.4 Overview of calculated band gap values for kesterite and stannite reported in Reference

Reports on the temperature dependence of the band gap of CZTS are very scarce, especially at low temperatures. The few reports that exist do not reach a consensus. In reference a band gap energy shift smaller than 10 meV was noticed from 22 to 300 K (3.6·10−5 eV/K). In reference the average band gap narrowing coefficient was 8.6·10−4 eV/K in the range 77-410 K estimated from transmittance data. At 10 K the band gap was about 1.64 eV. In reference the band gap at 10 K in a Cu-rich CZTS crystal was determined via the exciton emission peak leading to a band gap of 1.52 eV.

2.5 Electrical properties

The commonly observed conductivity of CZTS thin-films is p-type. Contrary to CIGS, the

dominant accepting defect the most easily formed is not VCu but the deeper CuZn anti-site defect according to references. Because this accepting defect is not as shallow as VCu, a carrier freeze-out could be an issue for CZTS concerning high-efficiency devices. References suggest that the copper vacancy is the dominant acceptor in Cu-poor and Zn-rich CZTS. The hole concentration was reported to vary from 1016 to 1018 cm^{-3} .

2.6 Defects

Information about defect activation energies is very scarce and the values determined in different reports are not similar. In general, experimental values indicate low activation energies while theoretical calculations rather point towards high activation energies.

CHAPTER III

3. First principles calculations

By first principles calculations it was found that the formation of point defects involving Sn is unlikely due to the covalent character of the Sn-S bonds. Cu and Zn are the most likely source of defects as their bonds are to a large extent ionic. First principles calculations in reference show that the acceptor defects which have low formation energy and lead to the p-type conductivity are CuZn, CuSn, ZnSn, VCu and VZn. The deeper acceptor CuZn has lower formation energy than the shallower VCu. First principles calculations in reference confirm that CuZn is the dominant acceptor. n-type doping is very difficult for CZTS due to the easy formation of compensating acceptor defects. The formation energy of charged acceptors decreases as the Fermi energy shifts upward and can become negative. The negative formation energy means these defects will form spontaneously, reducing the free electrons and pinning the Fermi level. This may be the reason why there are no reports on n-type CZTS material and donors have higher formation energy. The most likely donors are the ZnCu anti-site and Cui interstitial with higher formation energy.

The role of electrically neutral defect complexes is predicted to be important. The defect complexes have remarkably low formation energies and electronically passivate deep levels in the band gap. The formation energy of the neutral defect complex [Cu−Zn-Zn+Cu] is the lowest. This defect can also be regarded as the occupational exchange between Cu and Zn crystallographic sites which correspond to the structural disorder found in the kesterite phase.

Reference expresses some points of criticism on the previous theoretical studies. In this reference it was pointed out that the very low or negative formation energy calculated for CuZn in reference would imply that the material would always be metastable. Calculations performed in reference showed that none of the defects had negative formation energy and CZTS is considered as a thermodynamically stable material. Another point of criticism found in reference, is the assignment of CuZn as the dominant defect as this is in contrast with the Cu-poor and Zn-rich optimal growth conditions which would suppress the formation of this

defect. Most important defects in CZTS are, recording to reference, CuZn, ZnCu, ZnSn, SnZn, (Cum)Sn (m = 1-3), VCu, VS, and Cui. The SnZn anti-site and the defect complex (Cu3)Sn are identified as the dominant acceptor traps. The Cu-poor and Zn-rich conditions suppress the formation of the dominant defects. In figure 2.5 the differences between the transition energies of intrinsic defects in CZTS calculated by references and are shown.

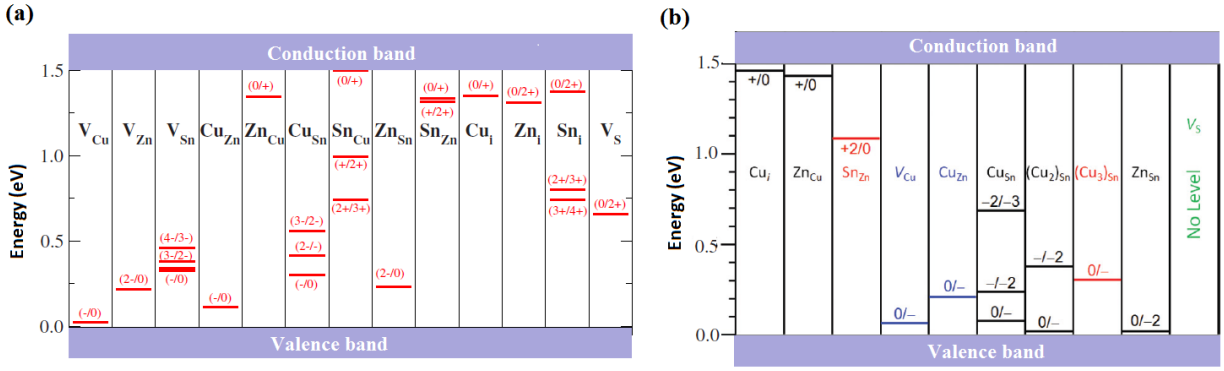

Figure 2.5 Ionization levels of intrinsic defect of CZTS following (a) reference, (b) reference .

3.1 Experimental results

Electric and optical spectroscopy measurements have been performed to find which are the dominant defects present in CZTS absorber layers. No agreement is reached.

In reference the origin of the p-type conductivity was ascribed to VCu based, on the composition of the single crystals which were made with a Cu-poor, Zn-rich and S-rich composition. In the work of reference it was found that the CZTSSe capacitance spectra exhibit a dielectric freeze-out to the geometric capacitance plateau. This step is attributed to a deep acceptor (Ea = 130-200 meV depending on Eg) which leads to a carrier freeze out resulting in a high series resistance at low temperature. It is stated that the large activation energy is consistent with theoretical studies which indicate that the dominant acceptor impurities are rather deep defects such as the CuZn anti-site. Other reports assign the capacitance step(s) directly to defects which are more shallow: a single defect with activation energy of 63 meV (attributed to VCu) is found for CZTSSe, in reference two defect levels are found (Ea = 120 and 167 meV) for CZTSSe and in reference two

defect levels (Ea = 44 and 112 meV) are revealed for CZTS by modelling an equivalent circuit to the admittance measurement.

Besides the assignments of a capacitance step to defects, a step in the capacitance spectra can also be explained by a parasitic effect. One step in the CZTS admittance spectra was seen and it was, by applying a simple circuit model, proven that an increasing series resistance with decreasing temperature can result in this capacitance step. In other words, parasitic effects distort the admittance spectrum. The secondary phase ZnSe has been attributed to be the cause of the series resistance. The findings of reference suggest that the interpretation of the admittance spectra should be handled with caution as an admittance step is thus not always related to defects.

Most PL studies on Cu-poor CZTS material show a broad peak around 1.3 eV. Two broad PL bands were detected in reference. PL measurements indicate that the material is strongly compensated which makes it very difficult to extract defect information from the PL measurements. Up to now there is no clear defect model which explains the origin of the broad PL band. Transition energies calculated from thermal quenching are rather small from 30-60 meV. Like for CIGS, only Cu-rich material provides narrow peaks in the PL spectra. Reports on Cu-rich CZTS are very scarce. The activation energies found in reference are ranging from 5-30 meV. Besides the assignment of the PL peak to defect transitions, a few reports mention the influence of other phases on the PL spectra.

3.2 Deposition

The CZTS solar cells investigated in this work are made by sputtering deposition of a precursor (Cu, Zn, Sn) and annealing of this precursor at an elevated temperature in an atmosphere of sulfur. The deposition step gives a homogeneous precursor film with full chalcogen content. The short anneal allows the film to crystallize into CZTS. This two step method is a more successful fabrication process compared to a single-step vacuum deposition process. A single-step vacuum deposition (typical for CIGS) at high temperature is not well-suited as CZTS material has shown a tendency to decompose when high temperatures (needed for annealing) are combined with low pressures (during deposition).

During the sputtering, atoms of a target (source material) are knocked out by bombarding ions of a working gas introduced in the evacuated chamber. The atoms are transferred to a substrate where they adhere. The substrate is thus coated by a thin-film. The target is the cathode, the substrate is the anode. The working gas is argon because it is a noble gas with low ionization energy and it is not expensive. Sputtering with direct current voltage works only for conducting materials. In the case of insulating materials, the surface charges because of the charge transferred by the argon ions. To avoid this problem, alternating current voltage is used (e.g. for ZnO sputtering). A magnetic field is applied (magnetron sputtering) in order to confine the electrons in the target's vicinity whereby the electrons then suffer more collisions with argon atoms which can lead to higher deposition rates and can reduce the substrate heating.
If several targets are sputtered at the same time (Cu, Zn, Sn) this is labelled as co-sputtering. An homogeneous mixture of several compounds can be achieved in this way. The investigated samples are sputtered in a H2S atmosphere. After the precursor deposition an annealing is applied (with or without additional sulphur).

In reference. The large line width of the PL spectra indicates that the material is strongly compensated. Another indication of the presence of potential fluctuations is the PL peak shift to higher energies with increasing excitation power. As a result of the compensation, Below the results of the investigations concerning the defect structure of CZTS thin-film solar cells by means of PL measurements are described. Additional information about the separation of the band edge and PL emission was provided by PLE measurements. Three reactively sputtered CZTS thin-film solar cells are investigated which differ in absorber layer (different sputter targets and annealing step) or buffer layer thickness. Device performances of the cells are compared as well as their morphology and composition.

3.3 Preparation and performance

Cell preparation The CZTS thin-film solar cell structure is presented in figure 3.1. Substrates were prepared by direct current sputtering of Mo (350 nm) onto cleaned soda-lime glass slides. CZTS precursor films were deposited on the Mo layer by reactive pulsed dc magnetron cosputtering of Cu, Sn and Zn in an H2S atmosphere. The thickness of the absorber layer is around 2 _m. The CdS buffer layer (50 nm) is deposited by CBD. The window layer of ZnO (90 nm)/ZnO:Al (350 nm) was deposited by RF-sputtering, the contact grid Ni/Al/Ni (3 _m) by evaporation. The previous description applies for all cells; sputter targets, annealing step and buffer layer thickness are different and will be described below.

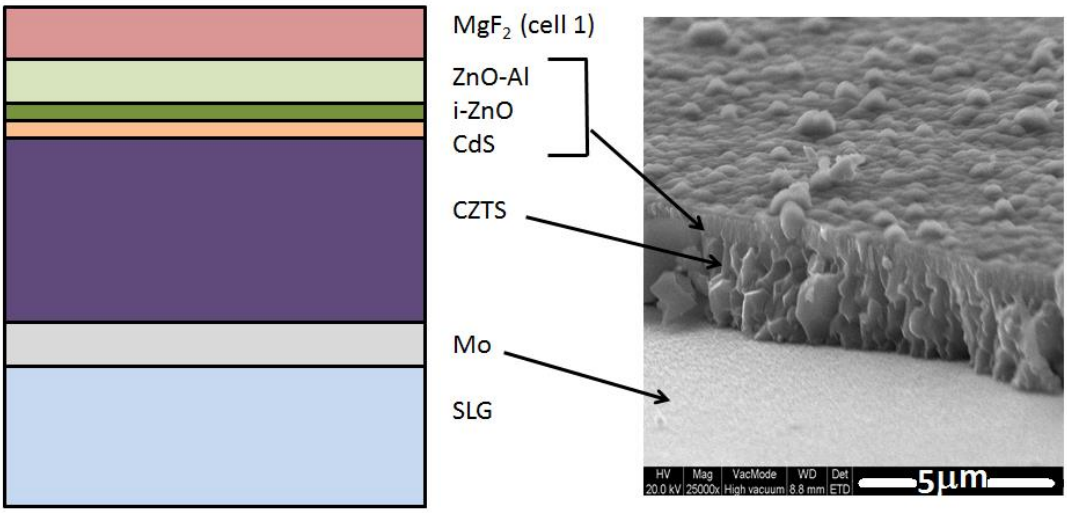

Figure 3.1 Left: cell structure, right: SEM image of cell1.

Cell1 is deposited by co-sputtering using metallic Cu:Sn (2:1) alloy and pure Zn targets in an atmosphere of H2S. The precursors were annealed, face-down on glass, in a tube furnace under a static argon atmosphere without added sulfur for 3 minutes at 550_C (for more details see reference). This cell has an additional MgF2 anti-reflection coating (105 nm).
Cell2 and cell3 have the absorber layer in common with each other but differ in buffer layer thickness. The absorber layers are reactively sputtered in H2S atmosphere using Zn and Cu:Sn (65:35) alloy targets. The samples are subsequently annealed in a sulfur atmosphere (graphite

box) for 10 min (for more details see reference). For cell2 the CBD was performed once. For sample cell3 the CBD was performed twice, which leads approximately to a double thickness. In experiments with repeated CdS depositions on glass, it has been seen to produce around double the thickness as determined by measuring the Cd intensity in XRF. The differences between all cells are summarized in table 3.2.

Table 6.1: Difference between investigated cells.

		Anneal		
	AR MgF_2	time (min)	S atmosphere	CdS thickness (nm)
cell1	yes	3	no	50
cell2	no	10	yes	50
cell3	no	10	yes	100

Table 3.2 Difference between investigated cells

Solar cell device parameters Cell performance characteristics can be found in table 3.3. The I-V curves of cell2 and cell3, measured just after the production of the cells, are visible in figure 3.3.

Table 6.2: Cell performance characteristics of CZTS solar cells (numbers provided by Uppsala University).

sample	η(%)	V_{oc} (mV)	J_{sc} (mA/cm^2)	FF (%)
cell1	3.50	528	16.6	43.4
cell2	6.05	657	14.8	62.3
cell3	5.62	652	14.5	59.3

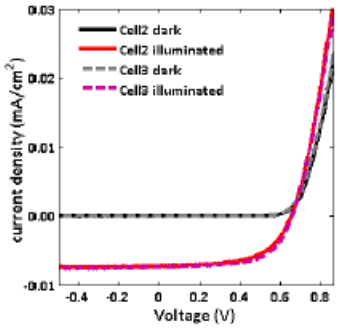

Figure 6.2: Illuminated and dark I-V curves of cell2 and cell3 (Uppsala university).

Figure3.3 Illuminated and dark I-V curves of cell2 and cell3

3.4 Spectral response

EQE measurements were performed without background illumination at room temperature in

collaboration with ELIS (department of Electronics and Information Systems at Ghent University).

Because some scratches were made on the samples, EQE measurements were performed on a limited surface. Therefore, the intensity could be hindered by some shadowing. For a comparison the normalized spectra are shown in figure 3.4. The EQE spectra give information about the difference in absorption at the long wavelength side and about the effect of the buffer thickness at the short wavelength side.

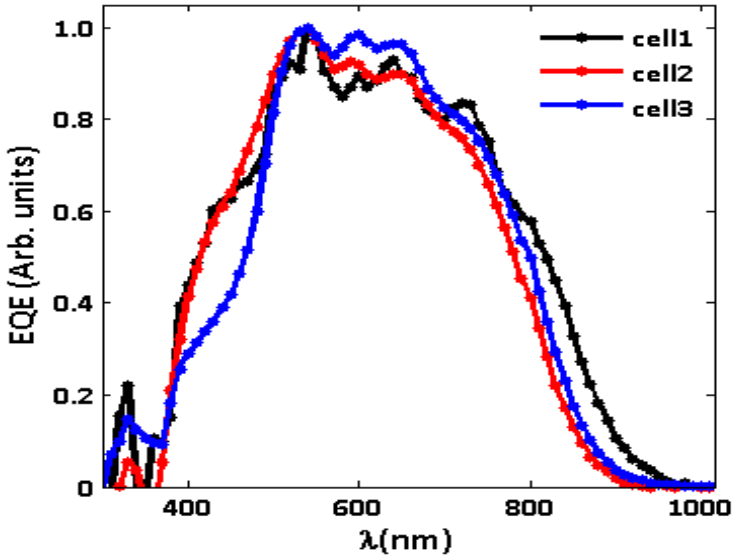

Figure 3.4: Normalized EQE of CZTS solar cells.

3.5 Long wavelength side: band gap determination

In the case of an ideal solar cell, the quantum efficiency would be a step function that is unity for all wavelengths below the wavelength corresponding to the absorber band gap and zero above.

The non-abrupt cutt-off is visible in figure 3.4. A linear extrapolation of the squared EQE yields a rough estimate of the band gap at room temperature. As the absorber layer is the same for cell2 and cell3, the band gaps are, within experimental error, identical; Eg = 1.49 ± 0.03 eV for cell2 and Eg = 1.46 ± 0.03 eV for cell3. The values are close to the band gap expected for of CZTS (_ 1.5 eV). The onset of absorption for cell1 lies at longer wavelengths.

This difference can be caused by different annealing process and related composition differences as shown in references. The latter cannot be confirmed by EDX measurements as no clear difference in elemental composition is measured. The band gap of cell1 is estimated as Eg = 1.41 ± 0.07 eV.

3.6 Short wavelength side: effect of buffer layer thickness

As a result of a doubled thickness of the buffer layer in cell3, the EQE in the short wavelength region (400-500 nm) is lower compared to cell2, because more light is absorbed in the thicker buffer layer. This optical loss at short wavelengths for cell3 results in a lower efficiency (5.62%) compared to cell2 (6.05%). From around 500 nm the EQE curves of the two cells cross. This means from excitation wavelengths of 500 nm there will be good absorption (EQE 81%) in the absorber layer.

3.7 Morphology

By SEM images an idea of the absorber quality and morphology can be obtained (figure 3.5). For cell1 the MgF2 layer is visible above the ZnO window layer. In none of the cells the CdS buffer layer is distinguishable. The morphology of the cells is quite similar, small grains are present.

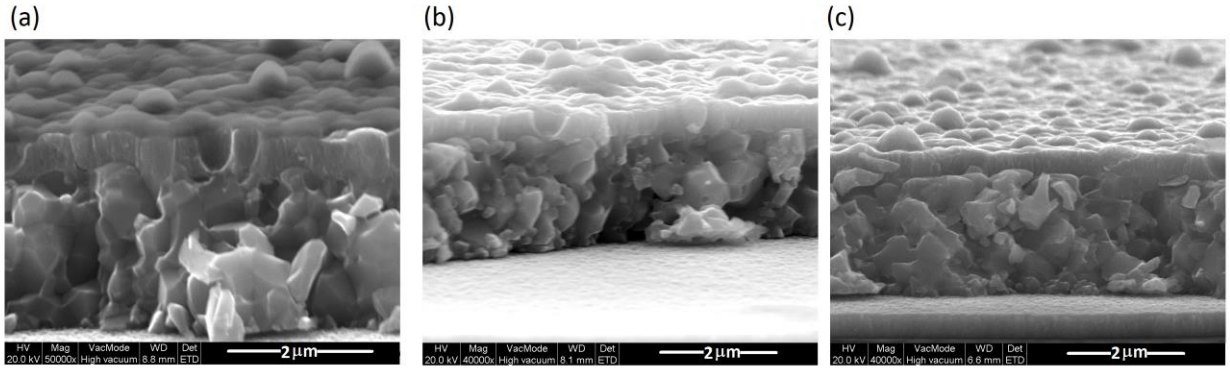

Figure 3.5: SEM images of the investigated cells (a) cell1, (b) cell2, (c) cell3.

3.8 Composition

3.8.1XRF

The metal composition of the non-annealed sample (precursor film) is measured with X-ray fluorescence spectroscopy (XRF), calibrated with Rutherford backscattering. Numbers were provided by Uppsala University. The results of the measurements performed at samples from the same run ('sister piece') are presented in table 6.3 and show that all precursor films have a slightly Zn-rich composition.

Table 6.3: XRF measurements on CZTS precursor films (numbers provided by Uppsala University).

	Atomic percent			Ratios	
Sister piece of	Cu	Zn	Sn	Cu/(Sn+Zn)	Zn/Sn
cell1	0.46	0.28	0.26	0.84	1.1
cell2 and cell3	0.47	0.29	0.24	0.89	1.2

Figure 3.6 XRF measurements on CZTS precursor films (numbers provided by Uppsala university)

For cell1 no composition information after annealing is available, cell2 and cell3 are measured with EDX after annealing. By comparing the EDX measurement with the XRF measurement on the precursor sample, a shift between EDX and XRF is calculated. The EDX measurement performed after annealing, was calibrated by this value. Measuring with EDX (acceleration voltage 20 kV) from the top on the annealed samples, calibrated against XRF, shows that a small amount of Sn is lost, giving a stoichiometric Cu/Sn ratio, while the Zn-excess is not changed (Cu/(Sn+Zn) = 0.91 and Zn/Sn = 1.2). Sulfur composition after annealing of glass/Mo/CZTS samples is difficult to measure because the sulfur and molybdenum peaks in the EDX spectrum are not easily distinguished as an overlap exists between the sulfur K lines and the molybdenum L lines at about 2.3 keV. Therefore the acceleration voltage was reduced below 12 kV in order to reduce the penetration depth whereby Mo is not detected. By reducing the acceleration voltage the Zn peak is not visible any more.

A reference sample without Mo, which consists of CZTS deposited on Si, is made in the same run. A comparison of S/Sn on the Si/CZTS reference sample and glass/Mo/CZTS is possible and is performed for cell2 and cell3. The overall S content is around 50% in these samples. In conclusion, EDX/XRF measurements show that the samples are Zn-rich.

EDX - Difference in S composition between cell1 and cell2

EDX line scan measurements (performed in collaboration with Lumilab, research group of the department of Solid State Sciences at Ghent University) of SK, CuK, ZnK, MoL, SnL and MgK lines are performed on a cross section of cell1 and cell2 (figure 3.7). To separate the Cu and Zn signals (their L lines at lower energy are very close), the acceleration voltage must be high (15 kV), which implies lower spatial resolution.

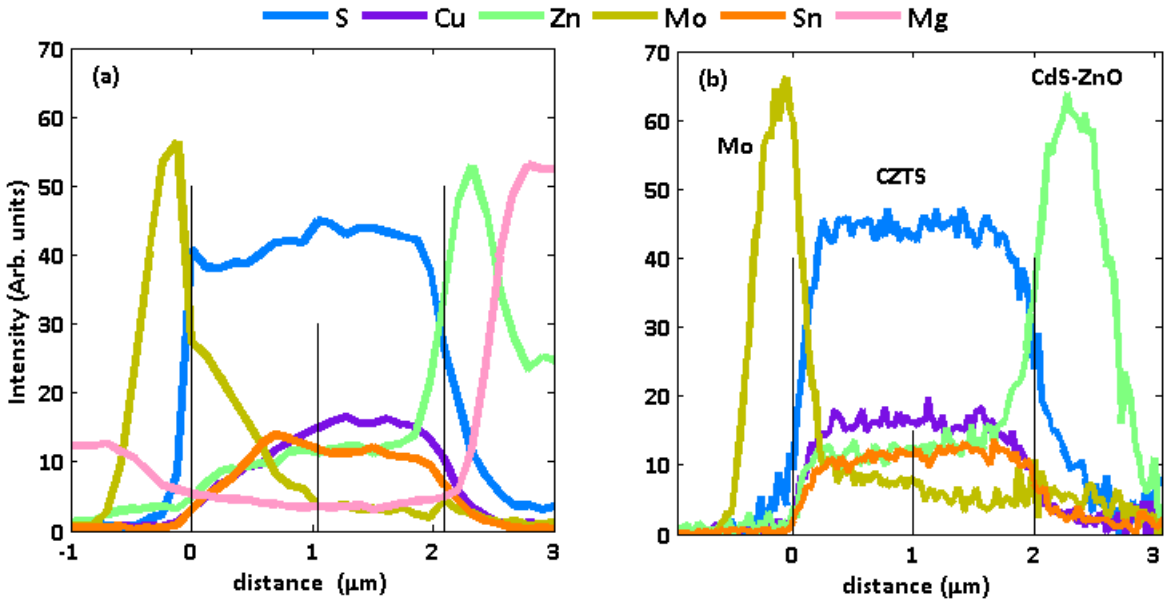

figure 3.7 EDX line scan measurements of (a) cell1, (b) cell2. Black lines indicate begin, middle and end of the absorber layer.

Because of a high number of different elements in the solar cell, the specific geometry of the sample (signals from Mo and ZnO layer near absorber could overlap with S and Zn signals coming from the absorber layer) and overlapping peaks, it should be stated that the concentration results are only semi-quantitative and will only be used to investigate if there is a large influence of the different annealing step in H2S between cell1 and cell2. No absolute values concerning the composition will be used from these measurements. Spectrum

corrections have been applied in order to obtain semi-quantitative concentration values. This includes subtraction of the background and calculation of the number of counts for each element by measuring the areas of the X-ray peaks of each element. When peaks are overlapping, peak deconvolution is applied.

The number of counts is subsequently converted into elemental concentrations by comparison with a standard and taking into account a sensitivity factor. As overlapping Mo and S signals hinder a correct measurement at the back of the absorber layer, ratios between different elements are calculated in the first half of the cell (surface region).

Although the annealing for both cells was different, the S/(Cu+Zn+Sn) ratio is approximately the same for both cells as visible in figure 3.8. From the EDX cross sections it could be concluded that the difference in annealing does not lead to a clear composition difference between the cells.

Table 6.4: Composition ratios between cell1 and cell2 determined from EDX.

sample	Cu/(Zn+Sn)	Zn/Sn	S/(Cu+Zn+Sn)
cell1	0.68	1.07	1.11
cell2	0.65	1.10	1.09

Figure 3.8 Composition ratios between cell 1 and cell2

CHAPTER IV

4.Photoluminescence

4.1PL emission

Position dependence and fitting procedure

The PL spectra of the CZTS cells consist in most cases of a very broad peak without any substructure which makes the interpretation rather difficult. However, differences in shape between the spectra exist as result of differences in relative intensity of individual peaks, which can be related to spatial variations within the cells. The variations in peak intensities in the spectra can also be obtained by changing the sample position with respect to the excitation spot. By slightly rotating the sample or shifting it in the vertical position, another spot on the sample is illuminated or the horizontal penetration depth can be altered as illustrated in figure 6.6 (the possible effect of interference will be discussed in section 6.6). The variations in individual peak intensities are an important aid to verify if a correct fitting is reached.

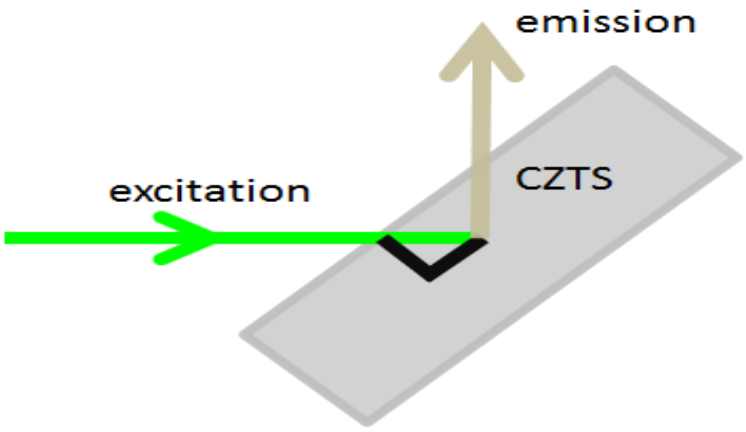

Figure 4.1 Position of sample relative to excitation and emission light.

The PL spectra (of CZTS as wells as of CIGS) can be decomposed in multiple, broad Gaussian components (a·exp(-((x-b)/c)2), with a the amplitude parameter, b the peak position and c the peak width parameter). In the fitting procedure, a shift of maximum 3 meV for each component between different cells, was allowed as the emission peaks can shift relative to each other

because of a change in temperature, excitation power and defect density for DAP recombinations.

If the donor or acceptor density decreases, the average separation increases, which reduces the Coulomb term and lowers the emission energy. The fitting is applied on normalized spectra in which the background is subtracted, the intensity and peak width of each component is kept variable. The fitting is first performed on the spectra which reveal most substructure. In order to check if the fitting is correct, the fitting is, keeping the energy positions fixed, applied to other spectra measured at different positions/excitation angles. As excitation wavelength dependent measurements in some cases reveal a decrease or increase of some components, the accuracy of the fitting is further checked on the excitation wavelength dependent spectra. In the last step, temperature dependent spectra are fitted. At higher temperature these spectra reveal, in some cases, more clearly the contribution of individual peaks. In the fitting of the temperature dependent spectra a certain decrease of the PL peak energy as temperature increases (band gap decrease and/or red-shift as a result of potential fluctuations) is taken into account. In the fitting of PL spectra of different cells/samples, the whole series of peaks is shifted to higher or lower energy. The fitting error on the energy position of each Gaussian component is estimated in the order of 5 meV.
For cell2 and cell3 it is rather straightforward that same defects would appear because the absorber layer is made in the same run. As the composition of cell1 is not very different (Table 3.2) the assumption that same transitions could appear, is investigated. As the PL spectra of cell1 lie at lower energy, the energy positions of the fitting for cell2 are shifted towards lower energy. The intensity and the broadness of the peaks could vary. It is found that the spectra of cell1 could be fitted with the same energy separation between the peaks as for cell2.

4.1.1Position dependence cell3

A description of the cell which showed the clearest individual contributions will be given first. Figure 4.2(a) shows spectra of measurements of cell3 performed at different positions and at

different openings of the excitation monochromator slits. In the low intensity spectrum two main peaks can easily be distinguished. The distinction between the two peaks disappears as the PL intensity increases. The spectra can be fitted with the same three Gaussian peaks (figure

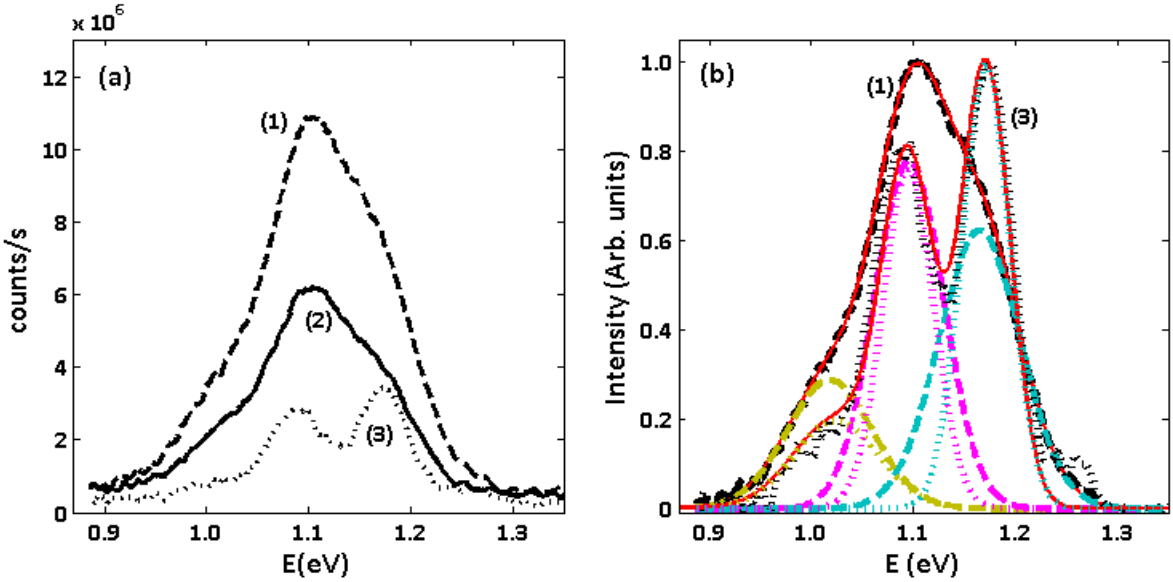

Figure 4.2 (a) PL spectra of cell3 at different positions (exci = 500 nm, T = 10 K), (b) normalized and fitted spectra of position (1) and (3).

4.1.2Position dependence cell2

In figure 4.3 the spectra of cell2 (measured with different set-up and hence different positions) are shown. Only a small dependence on the sample position can be noticed. Both spectra can be fitted with the same three Gaussian peaks as applied for cell3.

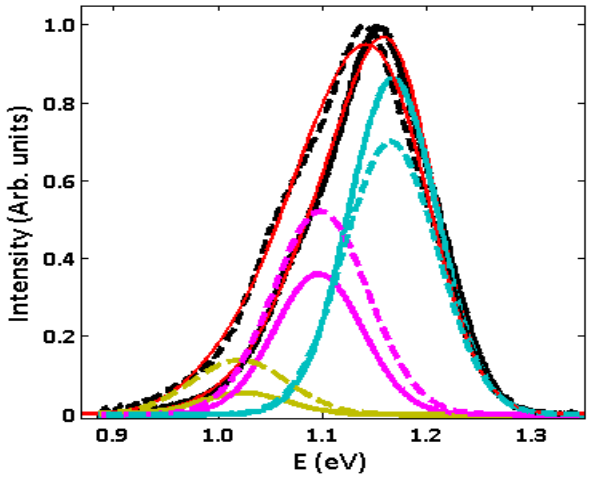

Figure 4.3: Spectra of cell2 at different positions (exci = 500 nm, T = 10 K).

4.1.3Position dependence cell1

Figure 4.4 shows the emission spectra of cell1 which are recorded with a Xe arc lamp lamp and an argon laser for excitation. The spectra look very different as sample position is changed. Again three Gaussian peaks suffice to fit the spectra. Peak 1 is more pronounced for position 1, peak 2 is more pronounced for position 2. It is this position dependence that made it possible to distinguish the contributions.

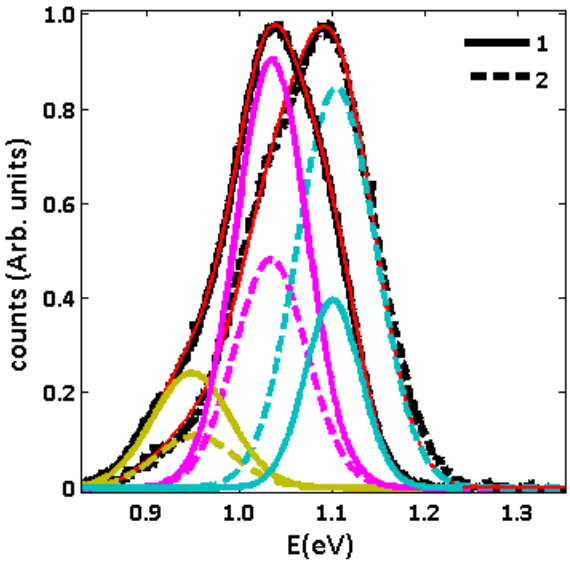

Figure 4.4 PL spectra at 5 K for cell1 measured with different excitation source. Position 1: laser (exci = 514 nm) Position 2: lamp (exci = 550 nm).

4.2Comparison PL spectra of different cells

The spectra of all cells at low temperature are compared in figure 4.5. The spectrum of cell1 is shifted over around 60 meV towards lower emission energy compared to the spectra of cell2 and cell3. This is in accordance with the lower band gap energy extracted from EQE measurements for cell1. Cell2 and cell 3 have the same absorber layer therefore the emission appears in the same energy region (figure 4.5(b)). In none of the spectra phonon replicas or any structure in the exciton region can be seen. Each spectrum shows broad emission bands which are an indication of fluctuating potentials in Cu-poor/Zn-rich material. The maximum of the

emission (around 1.04 eV for cell1 and 1.15 eV for cell2) appears for all cells at significantly lower energy compared to literature (normally around 1.3 eV). Another remarkable difference compared to literature is the appearance of three contributions in the spectra instead of one broad peak.

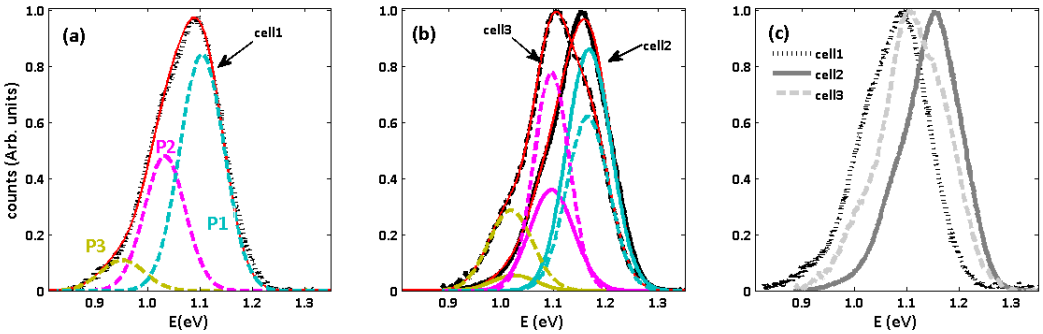

Figure 4.5 Normalized and fitted PL spectra

(a) cell1 (exci = 514 nm, T = 5 K, position 1),

(b) cell2 (exci = 550 nm, T = 10 K) and cell3 (exci = 500 nm, T = 10 K),

(c) Comparison PL spectra cell1-3.

All spectra can be fitted with 3 Gaussian peaks, labelled from high to low energy as P1, P2 and P3. From the fitting it is clear that the differences in shape of the spectra are a result of differences in relative intensity of individual peaks. The energy separations between the peak maxima is similar for the three cells as presented in table 4.6.

Table 6.5: Peak positions and difference.

	E_{max} (eV)			ΔE_{max} (eV)	
	P3	P2	P1	P1-P2	P1-P3
cell1	0.952	1.033	1.104	0.071	0.152
cell2	1.022	1.096	1.167	0.071	0.145
cell3	1.019	1.095	1.165	0.070	0.146

Figure 4.6 Peak position and differences

4.3 Excitation wavelength dependence of PL spectra

Excitation wavelength dependent measurements of cell2 and cell3 (figure 4.7) at constant low temperature reveal, in accordance with the EQE results, the effect of absorption by the buffer layer. Lower intensities for excitation wavelengths smaller than 500 nm are noticed for cell3 compared to cell2 and are an evidence of a thicker buffer layer of cell3. The ratios of the intensity maxima for excitation at 450 nm and 500 nm (absorption in buffer/transmission through buffer) are 0.43 for cell2 and 0.31 for cell3.

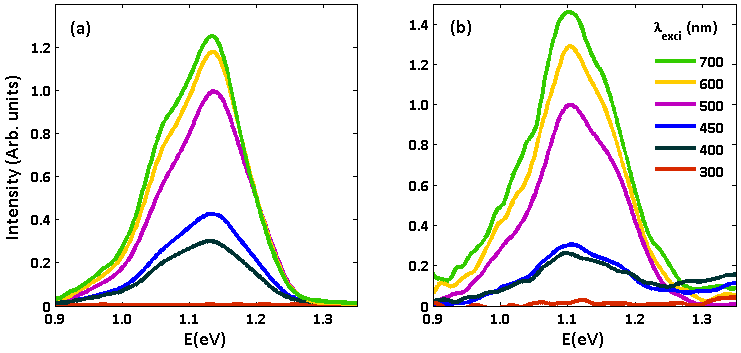

figure 4.7 Excitation wavelength dependent spectra normalized to the maximum of the spectrum at exci = 500 nm (T = 10 K) (a) cell2, (b) cell3.

4.4 Excitation power dependence of PL spectra

In excitation power dependent PL measurements on cell2 (figure 4.8(a)) gray filters were placed in front of the cryostat window in order to decrease the excitation power. The excitation power measured in front of the lens located in front of the cryostat (P0exci), was in the order of 290 mW/m2.

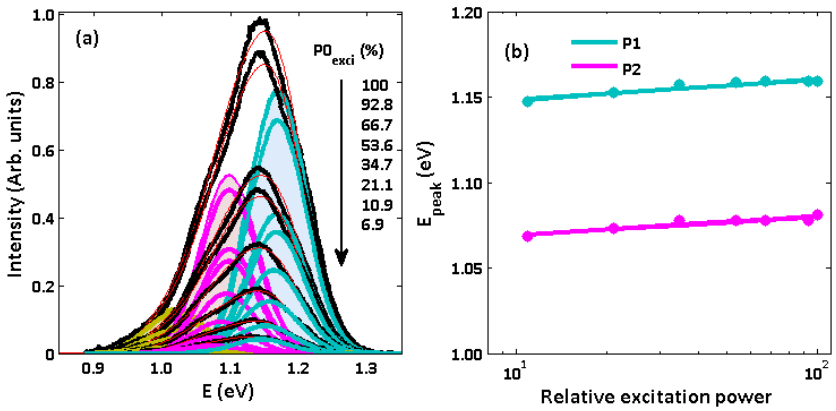

Figure 4.8(a) emission spectra of cell2 at different excitation powers (exci = 500 nm, T = 5 K), (b) emission peak energy of P1 and P2 as a function of excitation power.

The measurements exhibit a large blue-shift with increasing excitation power. The emission peak energy for peaks with highest intensities (P1 and P2) as a function of excitation power is shown in figure 4.8 (b). A linear fit according to Epeak = C + B·log(Pexci) gives as a result for B 11 ± 2 meV/decade of excitation intensity for P1 and 12 ± 2 meV/decade for P2. These rather large values are an indication of the presence of potential fluctuations in the material.

4.5 Temperature dependence of PL spectra

The emission spectra as a function of temperature for cell1 and cell2 are shown in figure 4.8. All temperature dependent PL spectra can be fitted with 3 Gaussian peaks. As the temperature for the detection of PL emission is limited to 70 K, no fitting of the temperature dependence of the peak intensity is made. Moreover, the interpretation of the fitting results is not straightforward because of different proposed fitting models and the effect of potential fluctuations.

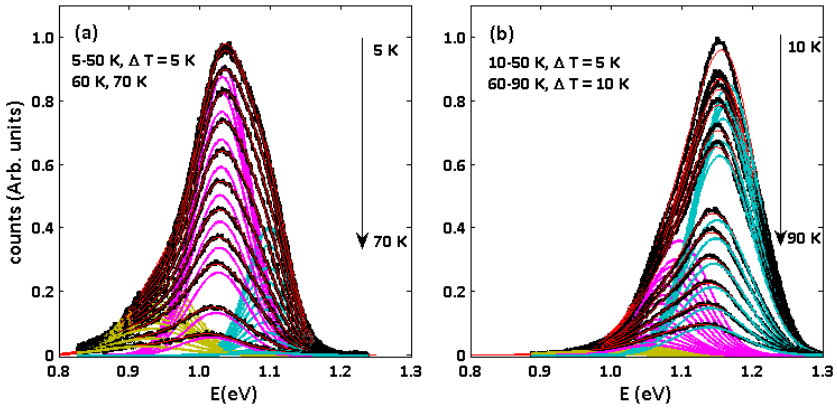

Figure 4.9 Temperature dependent measurement at λ_{exci} = 550 nm (a) cell1, (b) cell2

The red shift with increasing temperature can be related to the decrease of the band gap with increasing temperature but it may also be a result of potential fluctuations in the material . In material without potential fluctuations a blue-shift (or no shift) should appear with increasing temperature for DAP (free to bound) recombination . Reference states that the emission energy of a q-DAP transition shifts to lower energy as the temperature increases. For a tail-defect and band-tail transition a red-shift is expected for the emission energy.

A blue-shift with increasing temperature is expected for a band-defect transition. In the investigated temperature region, no change from a red-shift to a blue- shift, which could indicate a transition from tail-defect to band-defect recombination or from band-tail to bandband recombination, is visible. Moreover, for the latter transitions, the low energy signal is quenched in favour of the high energy signal. This is not clearly seen in the spectra of figure 4.9. The appearance of only a red-shift, the absence of red to blue-shift and absence of the strong quenching of the low energy signal favours the explanation of the emission peaks by q-DAP transitions. More information could be obtained if the PL signal could also be detected at higher temperatures.

CHAPTER V

5.Fabrication techniques

Fabrication of CZTS thin films in this study was performed by a two-stage process, sputtering a metal precursor or a metal-sulphur precursor, respectively, followed by a sulphurization process.

5.1Precursor deposition by sputtering

5.1.1Sputter process

To deposit the precursors on the substrate, the magnetron sputtering technique is applied. It is based on momentum transfer from bombarding ions of working gas to the target atoms. By this, the atoms are knocked out from the target and are transported to the surfaces. When they get in contact with a surface, the atoms adhere, for example on the substrate. As a result, the substrates get coated by a thin film of the target material.

5.1.2DC and AC sputtering

A sputter system is set up as follows. The target, i.e. the source of the used material, acts as the cathode and is connected to the several kilovolts high direct current (*DC*) voltage . The anode is the substrate holder, or even the whole chamber like in the system used here, and typically connected to ground. In the evacuated chamber, a so called working gas is introduced. Often – and thus also in our case – Argon is used for this, as it is a noble gas (i.e. not reacting with the sputtered atoms) with low ionization energy. Furthermore it is low-cost and has a suitable mass for the momentum transfer to the target. Then a glow discharge is initiated and maintained in the chamber when a critical voltage is reached. The argon atoms get ionized by the high voltage and the electrons move to the anode (and ionize on their way further argon atoms), while the positively charged ions are accelerated towards the target and there knock out atoms. The aggregate state where electrons and atoms exist separated from each other is called plasma.
Sputtering in this way with DC voltage works only for conducting materials. In

the case of insulating materials, the surface charges up because of the charge brought by argon ions. To avoid this problem, alternating current (*AC*) voltage is used. In our case, ZnS and ZnO required this approach.

5.1.3Magnetron sputtering

In magnetron sputtering, a magnetic field is applied in order to confine the electrons in the target vicinity. The electrons then suffer more collisions with argon atoms thus increasing plasma density. That makes possible to reduce the working gas pressure, which, in turn, lets more energetic particles reach the substrate and also results in higher deposition rates. Another positive effect of trapping the electrons near the target is reduced heating of the substrate.

5.1.4Co-sputtering

It is even possible to sputter several targets at the same time. This could be desirable to dope a material by co-sputtering an appropriate small amount of the doping material, or to achieve a homogenous mixture of several compounds. If a sufficient energy supply is given – for example by heating the substrate –, even crystal growth already during sputtering can be enhanced.

We used co-sputtering in order to reduce diffusion of the sputtered metals during sulphurization.

Chapter VI

6.EXPERIMENTAL

6.1kesterite CZTS films via Cu-Zn-Sn electrodeposition followed by sulfurization

6.1Experimental Details

Electrodeposition of Cu-Zn-Sn (CZT) alloy films was performed at room temperature in a three-electrode cell with vertical electrodes, the cathode and counter electrode facing each other. A Pt mesh was used as the counter electrode, and a saturated mercurous sulfate as the reference (MSE, EMSEo=0.650VSHE); in the following, all the potential will be referred to MSE. The experiments were performed using an EG&G-PAR potentiostat-galvanostat Model 263A. The CZT films were grown from an acidic solution (pH 2.3) combining 0.2 M C6H8O7, 0.2 M Na2SO4 30 mM SnSO4, 30 mM ZnSO4 and 40 mM CuSO4, using ultra-pure Milli-Q water (resistivity18.2 MΩ·cm) produced in house; pH was adjusted with diluted NaOH. The solution was filtered after the addition of SnSO4 and before pH adjustment. The working electrode substrate was a Mo sheet with 0.1 mm thickness and 99.95% purity (Alfa Aesar). The size of the sample was $\sim 1\ \mathrm{cm}^2$. Before deposition, the Mo foils were sequentially cleaned in acetone, isopropanol, and ethanol (30 minutes each), then etched in 25 vol% NH4OH solution for 3 minutes, rinsed and used immediately thereafter.

The sulfurization of the alloy precursors was performed at 500 °C or 550 °C for 1 hour in a sealed quartz tube using an Ar atmosphere. Sulfur pellets with 99.99% purity (Alfa Aesar) were used as the sulfur source. After annealing, the furnace was turned off, and films were naturally cooled, while still in the tube, down to room temperature in 12 hours, corresponding to an average cooling rate of ∼0.5 °C/min (note that temperature drop was not linear in natural cooling). No etching of secondary phases was performed.

A liquid junction cell was used to investigate the photoelectrochemical (PEC) response of the films, known to related to solar cell efficiency. PEC characterization was performed under simulated sunlight (Oriel Sol 1A, Newport) in a custom made cell using a 0.1 M Eu(NO3)3 (Alfa

Aesar) solution, brought to pH 2.3 with dilute H2SO4; the potential was scanned from −0.2 to −1.1 V with a 10 mV/s scan rate and the photocurrent was recorded using an SP 150 BioLogic potentiostat.

The crystal structure of the films was determined by X-ray diffraction (XRD), using a PANalytical X'Pert Pro MPD instrument with Cu Kα radiation (λ = 1.5406 Å) in a Bragg-Brentano configuration. The surface morphology of CZT precursor layers and CZTS films was examined with a FEI Quanta 650 Scanning Electron Microscope (SEM). The film composition was measured with an energy dispersive X-ray spectrometry (EDX) detector attached to the SEM; the accelerating voltage was 20 kV. Raman spectra of the CZTS films were acquired using a Renishaw inVia Raman microscope with an excitation wavelength of 514 nm or 785 nm with 3000 $\mathrm{mm}^{-1}$and 1200 mm^{-1}grating, respectively. The Raman spectrum of monocrystalline silicon was measured as a reference to correct the spectra with respect to the peak position 520 cm^{-1}.

6.2 Results and Discussion

This section consists of three parts; first, the electrodeposition of CZT precursor layers and their composition, crystal structure will be presented. Second, the influence of Zn/Sn ratio on the properties of CZTS films will be discussed, and lastly, the effect of sulfurization temperature on phase purity and PEC response of CZTS films will be compared.

Compositional and structural properties of electrodeposited Cu-Zn-Sn precursors The cyclic voltammetry (CV) for the Cu-Zn-Sn deposition solution is shown in Fig.1a. The voltammograms were run at a scan

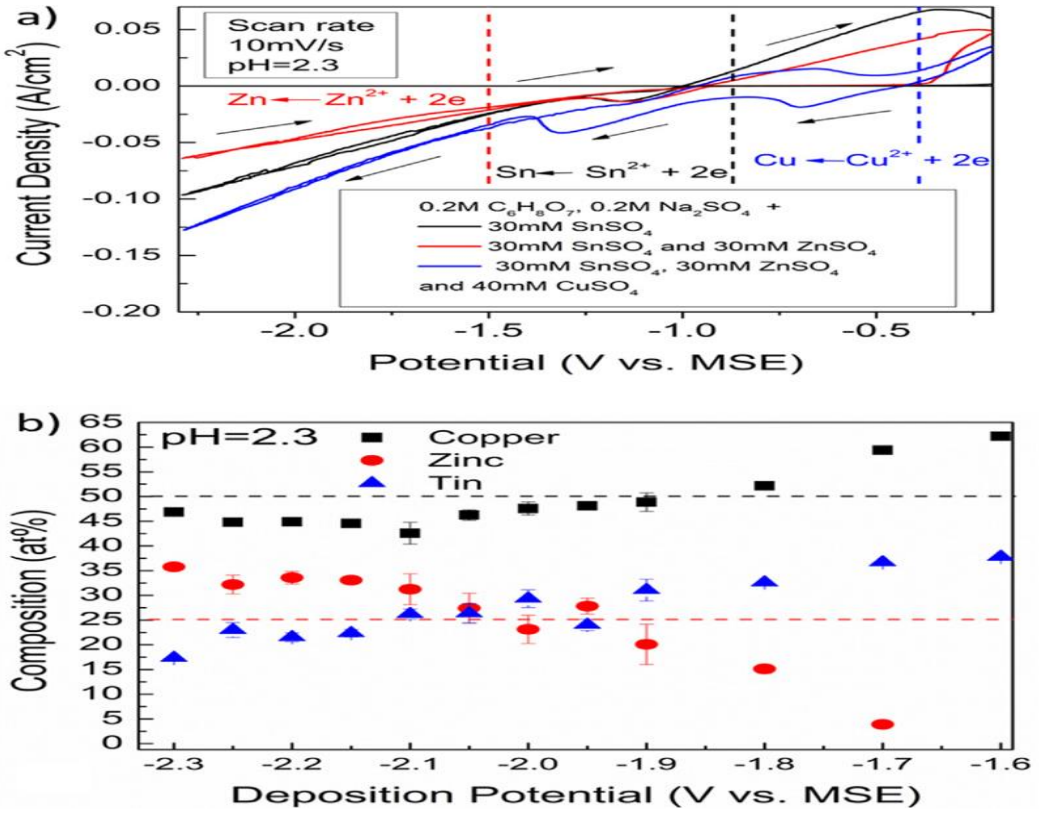

Figure 6.1 a) Cyclic voltammetry and b) composition vs. potential curves of Cu-Zn-Sn precursors.

rate of 10 mV/s. The calculated redox potential of copper, tin and zinc are -0.39,- 0.87 and -1.5 V, respectively. In comparison, the Cu reduction peak occurs around 0.7 V and the reduction of Sn starts at a potential of 1.0 V, showing significant over voltages. The reduction of Zn cannot be identified via CV since it occurs at potentials more negative than the hydrogen evolution reaction (HER). Fig 6. 1b shows the alloy compositional trend as a function of potential (deposition time 37–41 seconds) (Fig6. 1b). The fraction of Cu and Sn in the alloy decreases with higher over voltages. Zn was detected by EDS only at potentials more negative than 1.7 V, and its fraction increased at more negative potentials. The composition of the layers was measured at three different points on the samples. The compositional deviation was around 2.5 at% and was slightly larger for layers deposited at potentials more negative than - 1.8 V. A detailed lateral composition analyses for the metallic precursor can be found in S. Fig. 6.1 in the Supplementary Material. The alloy composition should be within a suitable range to enable the

transformation of Cu-Zn-Sn alloys into the CZTS phase during the sulfurization process. Relevant compositional ratios for Cu-Zn-Sn precursors are Cu/(Zn + Sn) and Zn/Sn; the stoichiometric ratio for the formation of CZTS films is Cu: Zn: Sn = 2:1:1, i.e. Cu/(Zn + Sn) = 1 and Zn/Sn = 1. However, record efficiencies for CZTS absorbers are consistently reported for Cu-poor and Zn-rich layers. This has been explained in terms of the facilitated formation of certain defects; stoichiometric and Cu-rich conditions tend to form shallow donor levels and mid-gap states, which are unfavorable for solar cell operation. Cu-poor and Zn-rich conditions in CZTS in contrast prevent the formation of detrimental defects. In this work, Cu-poor conditions were selected, while varying Zn/Sn ratios. Fig. 6.2a shows the composition of alloy precursors in the narrow potential range that is suitable for CZTS formation; note that the Cu fraction is similar for films with different Zn/Sn ratio. The lateral composition analysis of a CZTS later is provided in S. Fig.6.2 in the Supplementary material. XRD

Intermetallic compounds, Cu6Sn5 and Cu5Zn8, were detected, together with a small amount of elemental Sn. The XRD peaks for metallic Cu and Zn superpose with the intermetallic compounds reflections (2u _ 42_44_), making it difficult to detect and distinguish the relative amount of the various phases. Detailed XRD pattern investigation of Cu-Zn-Sn precursors and time dependent XRD patterns of a Cu-Zn-Sn precursor layer are shown in S. Fig. 3 and S.Fig 4 in the Supplementary Material. Fig. 6.3 shows planar and cross sectional SEM images for the Cu-Zn-Sn precursor electrodeposited at -2.05 V. The film (700 nm thick 190 nm) is continuous at the substrate side and less dense at its surface.

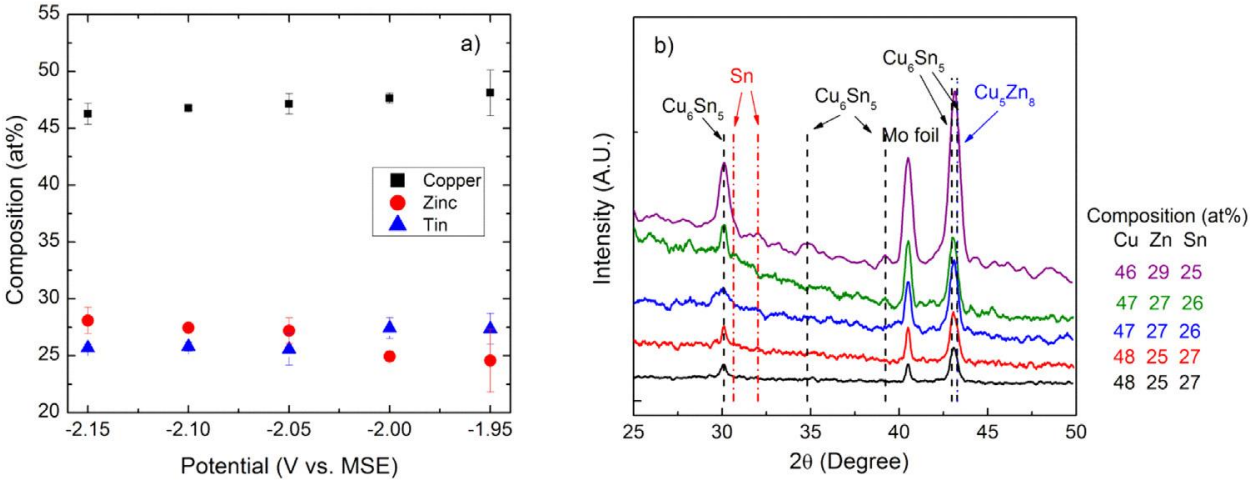

Fig. 6.2. a) Cu-Zn-Sn precursor composition and b) corresponding X-ray diffractometer patterns.

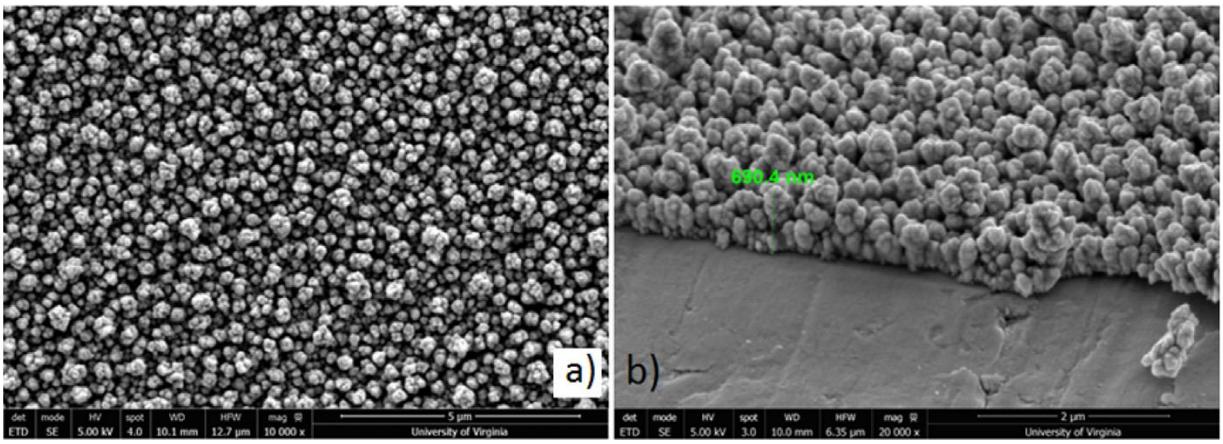

Fig 6.3. a) Top-down SEM image and b) oblique view showing the cross section, of Cu-Zn-Sn precursors electrodeposited at -2.05 V (vs. MSE).

6.3 Influence of Zn/Sn ratio of the Cu-Zn-Sn precursors on the formation of CZTS films

The composition of the CZTS layers after sulfurization as a function of applied potential is shown in Fig6.4 The fraction of sulfur in the films is ≈55 at %; note also that the initial Zn/Sn ratio changes after sulfurization (Fig6.5a). Specifically, after sulfurization at 500 °C Sn loss was observed for most of the samples, and Zn loss in one instance. The relative loss of Sn increases for more negative deposition potentials (Fig6.5b). Interestingly, we observed different elemental losses for metallic precursors characterized by the same Zn/Sn ratios, 0.93 or 1.04, which suggests a microstructure and phase constitution of the alloy dependent on applied potential. In the literature, compositional changes upon sulfurization are attributed to the loss of secondary phases. Initially binary sulfides (CuxSy, ZnS and SnS2) are formed below 300 °C and later, above 350 °C, these compounds react to form Cu-Sn-S phases. Finally, the CZTS phase is formed by the reaction of Cu2SnS3 with ZnS. During the formation of binary sulfides, solid tin monosulfide is forming by the desorption of sulfur-rich tin sulfides.

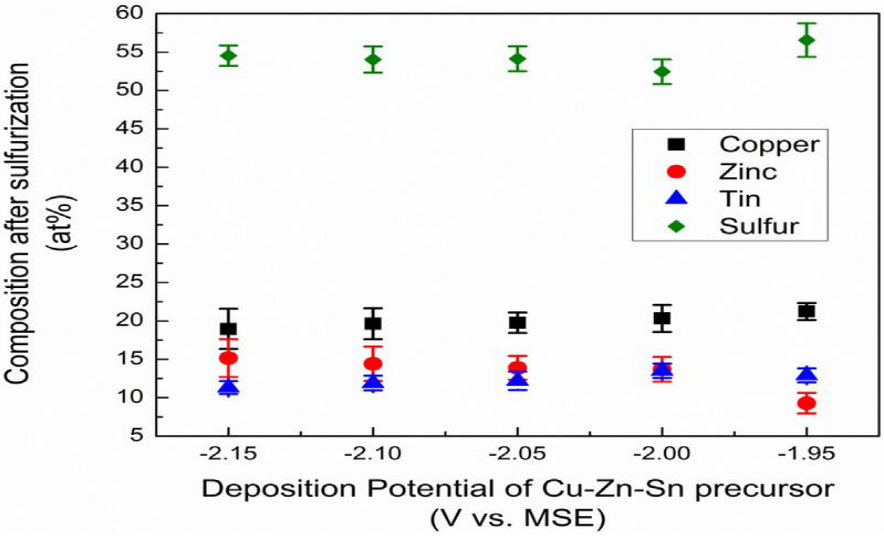

Fig6.4. Composition of CZTS films after sulfurization of Cu-Zn-Sn.

The evaporation of SnS(s) takes place between 350–450 °C, leading to a decrease in Sn concentration. The loss of Zn from CZTS layers has also been reported before and is attributed to the evaporation of elemental Zn before the formation of ZnS.

The X-ray diffraction patterns of CZTS films are shown in Fig 6.6 The reflections from the CZTS kesterite phase are indicated by the respective Miller indices; peaks around 2θ = 33, 47 and 56 degrees exhibit two sets of Miller indices due to the tetragonal peak splitting; the strongest Bragg peak (112) is observed for all films and is located around 2θ = 28.5. It must be noted however that this peak overlaps with the strong intensity peaks of most common secondary phases ZnS and Cu2SnS3. CuxSy phases were observed in most films; however, such peaks either disappeared or the intensity faded as the Zn/Sn ratio increased. In the literature, the presence of secondary phases for close to stoichiometric layers is often reported and is mostly due to the decomposition of CZTS at the surface. In our study, besides these secondary phases, SnS2 was also observed around 2 θ =50 for Zn/Sn ratios of 0.72 or 1.01, but not for higher Zn/Sn ratio. The XRD patterns of CZTS layers with relatively high Zn/Sn ratios (Zn/Sn = 1.14 _1.34) show slightly higher intensity superstructure peaks around 2 θ=16-18 degrees for (002) and (101). These two peaks do not overlap with any of the secondary phases, further supporting the increasing phase purity of CZTS.

Planar and cross-sectional SEM images of the CZTS layer with Zn/Sn ratio 1.34 are presented in Fig6. 7. These images show a continuous layer with grain size ranging from 100 nm to 650 nm and thickness of 1100 nm±300 nm. The bottom region of the film in Fig6. 7(b) shows smaller and more uniform grain size.

Better understanding of phase purity in the near surface region was achieved with Raman spectroscopy, enabling identification of most of the common secondary phases. Raman spectra of CZTS samples sulfurized at 500 °C and with different Zn/Sn ratios (0.72, 1.01, 1.34) were acquired with a 514 nm excitation wavelength and are shown in Fig6. 8a together with the theoretical Raman peak positions for kesterite CZTS (black lines) and some secondary phases. The two characteristic Raman modes for all CZTS films were observed around 334–339 cm^{-1} for the main A symmetry mode and around 287 cm^{-1} for the secondary main A symmetry mode. In Fig6. 8a the most intense peak is labeled as P1 and the peak for secondary main A symmetry mode is labeled as P2. The presence of these two features is strong evidence for a predominant kesterite CZTS material, because these peaks overlap the least with those of possible secondary phases in the Cu-Zn-Sn-S system. Significant shifts however were observed for both P1 and P2, and they are probably due to the presence of secondary phases and/or minor changes in lattice parameters. In order to better understand phase purity and crystal quality of the CZTS layers, it is important to investigate in detail the vibrational modes of each film. To this end, data fitting of the experimental data using the superposition of Lorentzian line-shapes was performed (Fig.6 8b–d). In Fig6.8b–d, besides the two main peaks for CZTS, other Raman modes contribute to a small extent to the spectrum, with Lorentzian line shapes centered at 253, 264, 274, 303, 316, 331, 347, 353, 366 and 373 cm^{-1}, attributed to E and B symmetry modes. The various lineshapes for the most intense Raman peak between 325 cm^{-1} and 340 cm^{-1} are shown with blue and red traces around 331 cm^{-1} and 337 cm^{-1}, attributed to the disordered and the ordered kesterite, respectively (Fig6. 8bd). In Fig6.8b, CZTS with Zn/Sn = 0.72, the most intense

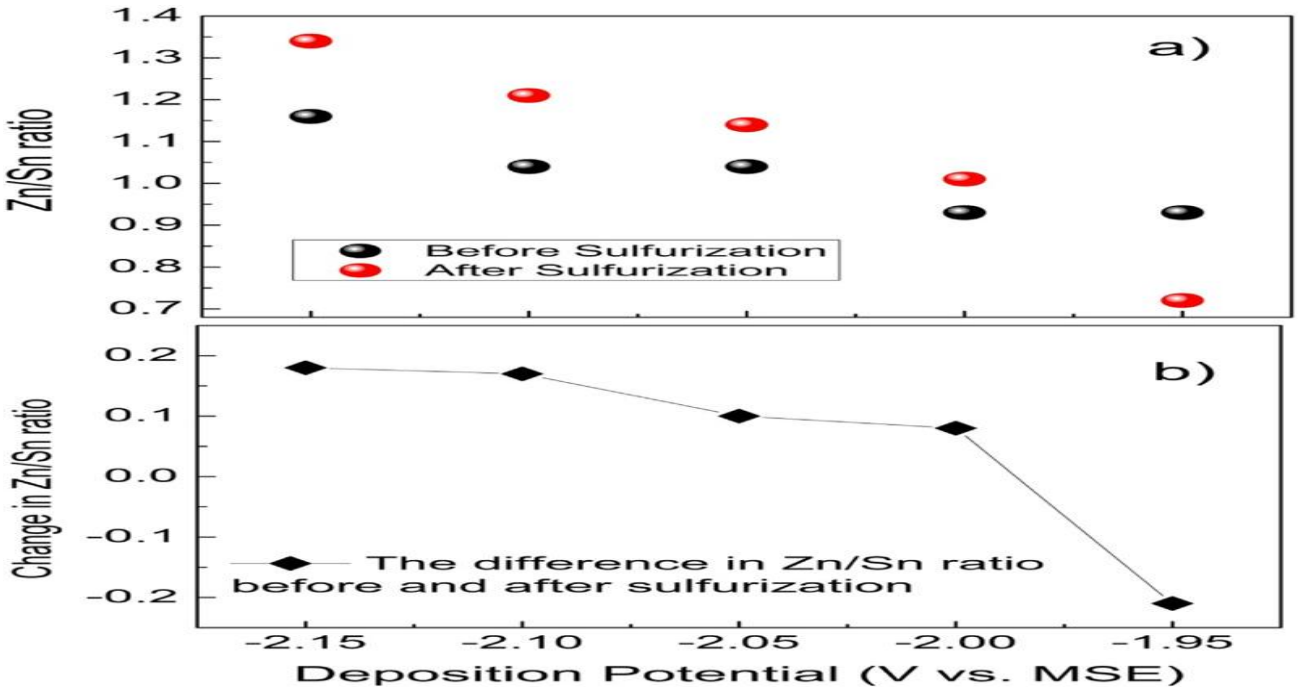

Fig6. 5. a) Zn/Sn ratio and b) Zn/Sn ratio change as a function of the deposition potential used to grow the precursor, before and after sulfurization at 500 °C

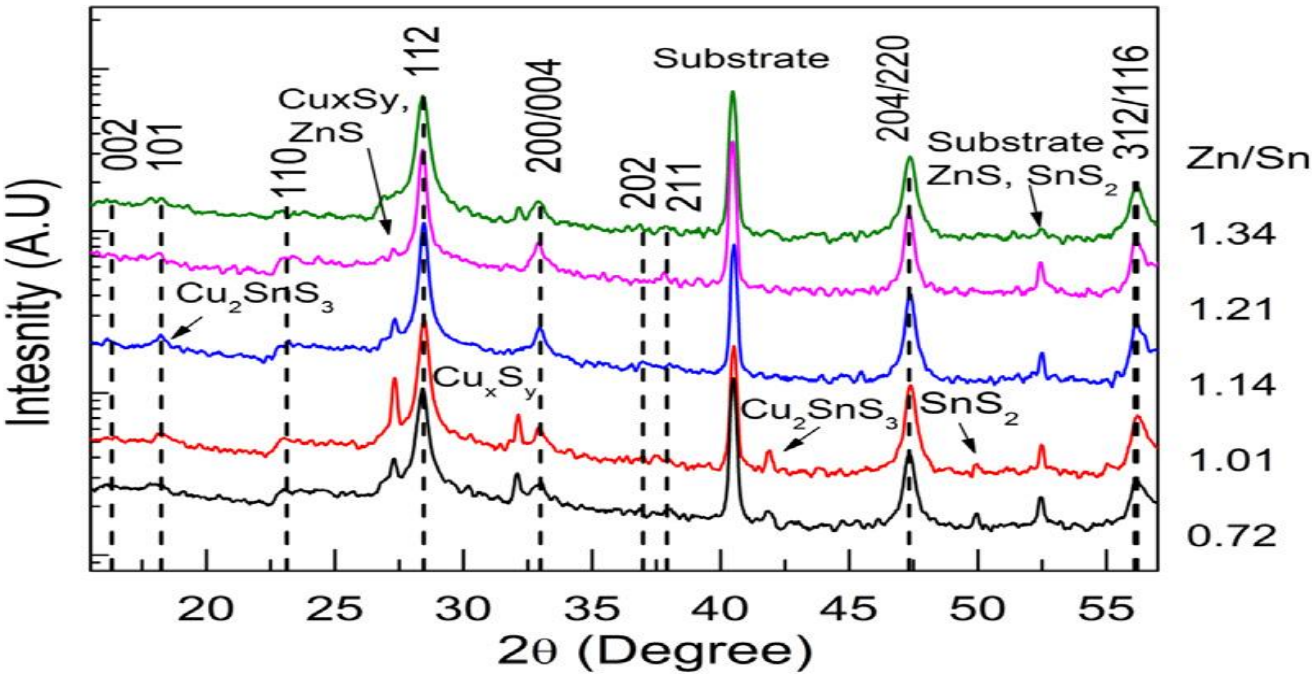

Fig. 6.6 X-ray patterns for CZTS films after sulfurization of Cu-Zn-Sn layers at 500 °C as a function of Zn/Sn ratio.

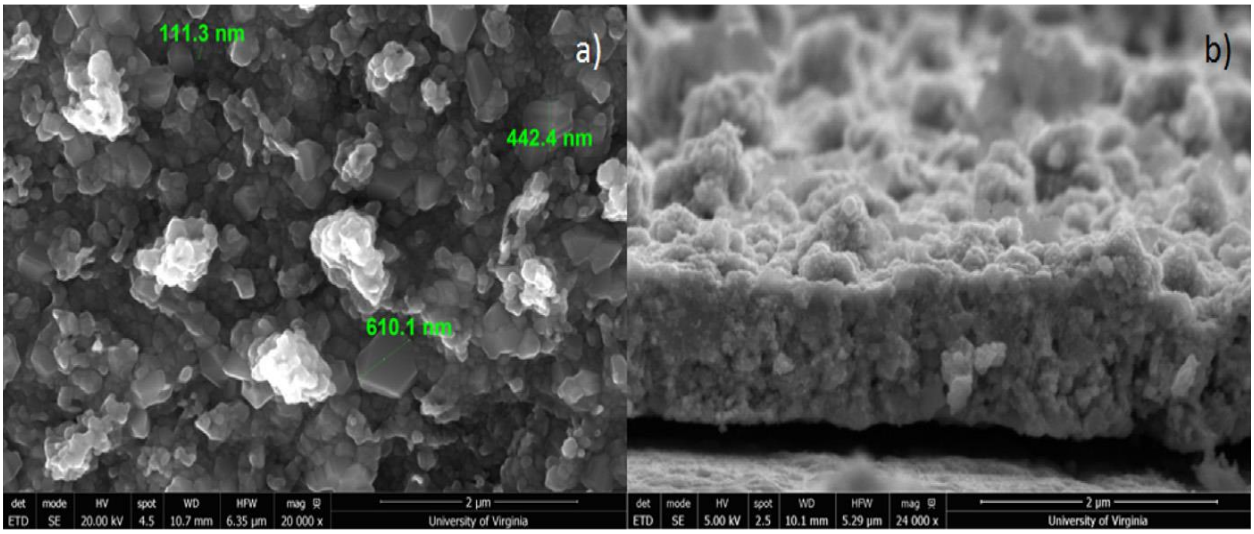

Fig6. 7. a) Top-down SEM image and b) cross section of CZTS film with Zn/Sn ratio 1.34.

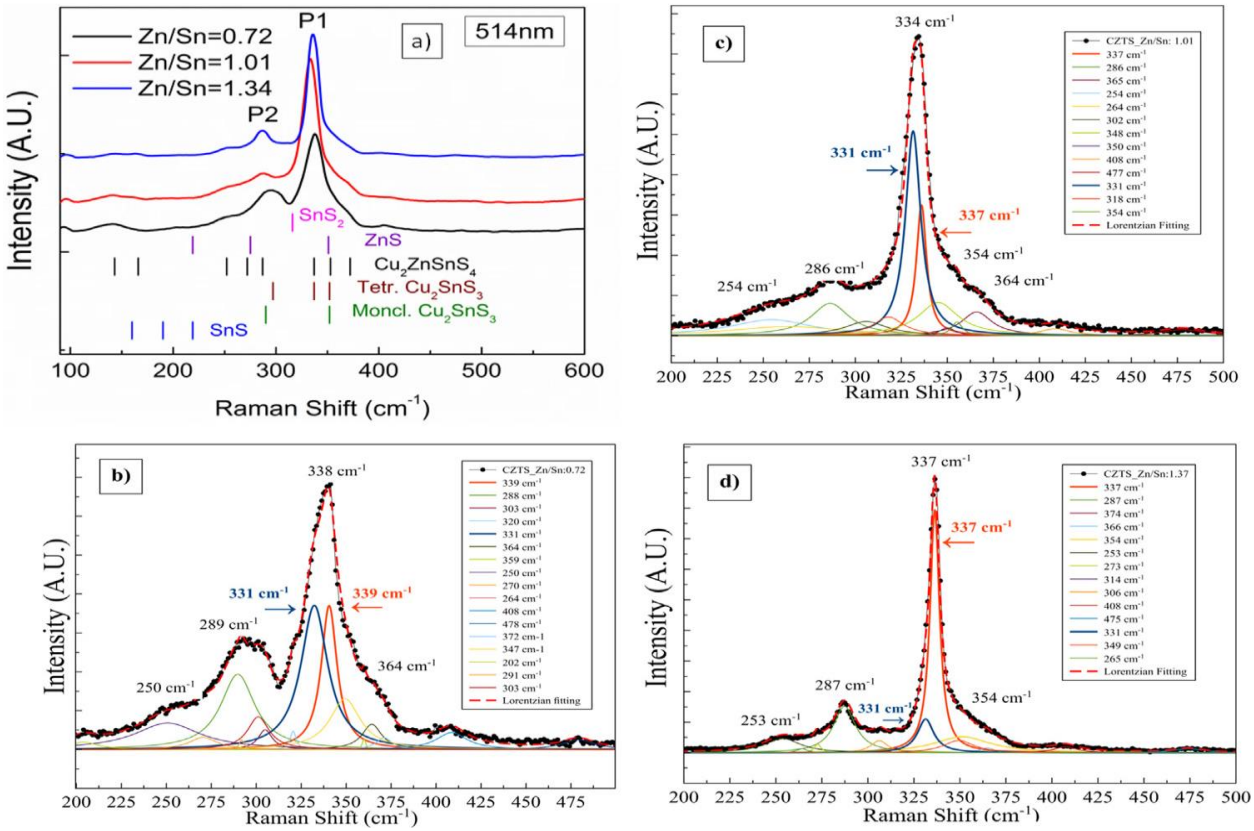

Fig6. 8. a) Raman Spectra for CZTS films and corresponding Lorentzian curve fittings for samples with b) Zn/Sn ratio 0.72, c) 1.01 and d) 1.34.

peak is centered at 338 cm^{-1}; the broad shape is due to the presence of disordered (331 cm^{-1}) and ordered kesterite (_339 cm^{-1}). The second most intense peak is located around 290 cm^{-1} (Fig6. 8b). This wide peak is attributed to the possible presence of secondary Sn-rich phases, such as SnS2 and Cu2SnS3, exhibiting Raman modes around 290 cm^{-1}, 314 cm^{-1} and 352 cm^{-1}. Since some of these peaks are either overlapping or very close to those of other phases, it is important to analyze X-ray diffractograms and Raman spectra in parallel. XRD patterns for the CZTS layer with Zn/Sn = 0.72 also show peaks from SnS2 and Cu2SnS3 phases (Fig. 6.6).

According to the fitting of Raman spectra, an additional feature besides the CZTS Raman modes around 320 cm^{-1} should be considered, as shown with a light blue line in Fig6.8b; this peak may be due to a minor ternary phase such as Cu3SnS4. The Raman spectrum of the sample with Zn/Sn = 1.01 is fitted in Fig6.8c. The most intense peak is around 334 cm^{-1}, and could be modeled with two Lorentzians centered at 331 cm^{-1} and 337 cm^{-1} for the disordered and ordered kesterite, respectively. Note that the relative intensity of the latter peak is lower in the Zn/Sn = 1.01
sample, suggesting a smaller fraction of ordered kesterite. The second most intense Raman mode is centered at 288 cm^{-1}; in contrast with the Zn/Sn = 0.72 sample, no peak could be found around 290 cm^{-1}, which suggests a significant decrease of the Cu2SnS3 phase fraction. The spectrum of the CZTS layer with Zn/Sn: 1.34, (Fig6.8d) instead matches well with all the theoretical Raman active modes for CZTS. The peak around 331 cm^{-1} (the disordered kesterite) has much lower intensity compared to the previous two films. A small intensity is observed for peaks at 408 cm^{-1} and 475 cm^{-1}, attributed to the MoS2 and CuxSy phases.The Raman spectra also show peaks corresponding to the MoS2 phase, which forms at the back contact upon sulfurization of metallic precursor. The chemical instability of CZTS and the Mo back contact has been reported before. The formation of this layer is unavoidable in absence of a passivating layer between Mo back contact and CZTS layer. Even without performing an etching process on the CZTS layers, only a small intensity was observed for CuxSy related phases. It is however important to note that the ZnS phase cannot be observed clearly with a 514 nm excitation

wavelength, and its presence cannot be completely discarded. As a whole, these data suggest improved purity of the kesterite phase at high Zn/Sn ratio.

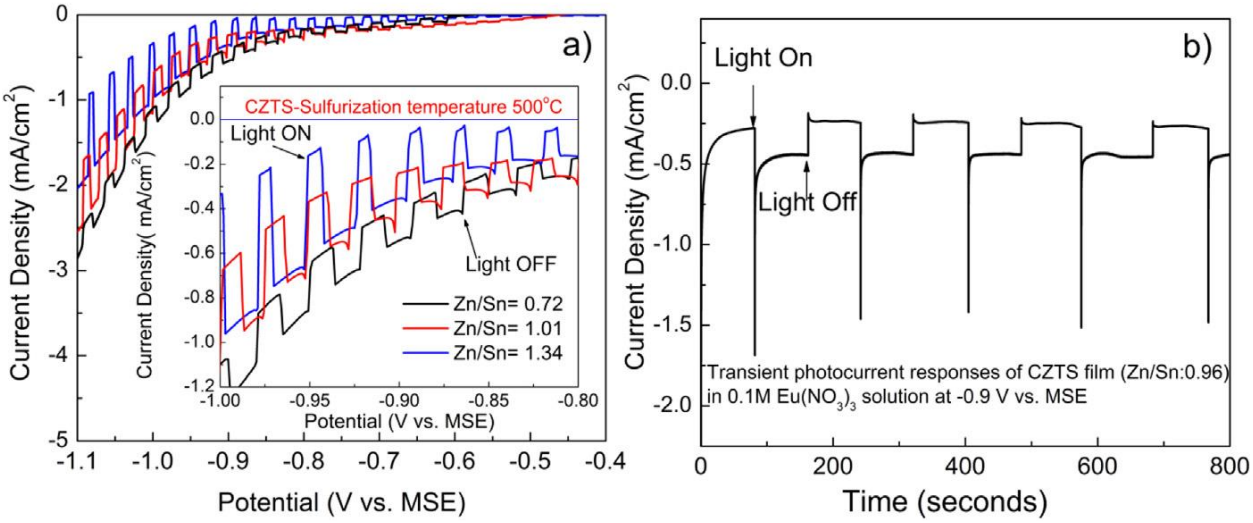

Fig6. 9. a) Photocurrent density vs. potential curves for CZTS films after sulfurization at 500 °C. The inset shows details in a window of more negative voltages and b) Transient photocurrent response of CZTS film at -0.9 V vs. MSE.

presence cannot be completely discarded. As a whole, these data suggest improved purity of the kesterite phase at high Zn/Sn ratio. Fig6. 9a shows the PEC response of CZTS layers sulfurized at 500 °C. The cathodic photocurrent of all CZTS layers gradually increased with decreasing applied potential, supporting the p-type conductivity of the films. The photoresponse of the films was greater with larger Zn/Sn ratio in the whole potential range. The PEC response of the CZTS layers at -0.95 V was between 0.23 and 0.51 mA/cm2. These values are similar to those measured at CZTS electrodes under similar experimental conditions in the literature. It should be noted however that, even though the Eu3+/Eu2+ redox couple is thermodynamically suitable to observe a photocurrent at CZTS, its kinetic properties are poor, leading to artificially low photocurrent values, as highlighted in a recent study performed on CIGS absorber layers. All the current-voltage curves show a significant dark current starting at about -0.85 V. This has been sometimes attributed to pinholes in the sample, but in this work we find that the dark current was larger in samples with relatively high fraction of secondary phases. The increase in dark current at more negative potentials may therefore be attributed to

electron-hole recombination and/ or charge carrier injection at the donor/acceptor interface. We used the measured photocurrent values after subtraction of the dark current to calculate the integral IPCE by using the maximum theoretical photocurrent density for a semiconductor with a 1.5 eV band gap under AM 1.5G illumination. The calculated values are between 0.82% and 1.82%. We examine also the photocurrent transient curve for CZTS layer with Zn/Sn ratio 0.96 after sulfurization at 500 °C (Fig6. 9b). The fast-current response upon illumination at -0.9 V suggests a low density of trap states, but the steep decrease afterwards evidences signifi-cant recombination. The on and off cycles in addition show a stable behavior for more than 800 seconds, suggesting that the Eu (NO3)3 solution is not damaging the CZTS layer within the time scale investigated.

6.4 Influence of sulfurization temperature on the properties of CTZS films

In this section, the influence of sulfurization temperature on the formation of CZTS films otherwise obtained under identical conditions is discussed. To this end, Cu-Zn-Sn precursor layers were sulfurized at 550 °C and the elemental losses were measured for samples with four different Zn/Sn ratio values, as shown in Fig6. 10; the Zn loss was more pronounced after sulfurization at 550 °C than at 500 °C (see Fig6. 5(b)). Top down SEM image of a CZTS layer sulfurized at 550 °C can be found in S. Fig6. 5 in the Supplementary Material.
X-ray diffraction patterns of CZTS layers sulfurized at 500 °C and 550 °C are compared in Fig6. 11. The strongest Bragg peak for both of the CZTS layers is again the (112); the intensity of the reflections however is much larger for the sample sulfurized at the higher temperature. No peaks from CuxSy or ZnS were detected for CZTS films with similar Zn/Sn ratio, after sulfurization at 550°C. We also observed the higher intensity superstructure reflections around 2θ = 16–18 degrees for the CZTS layer with Zn/Sn = 0.98 after sulfurizing at 550 °C (Fig. 11 red line), which were detected with much lower intensity for the CZTS layer with similar composition, Zn/Sn = 1.01, after sulfurization at 500 °C (Fig6. 11 black line).

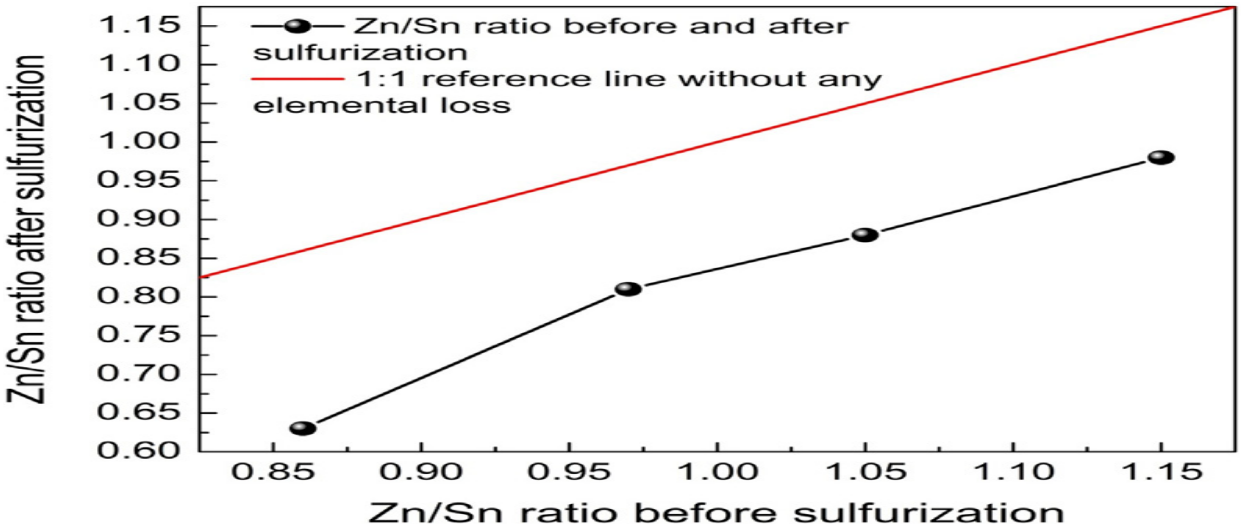

Fig 6. 11. X-ray patterns of CZTS films sulfurized at 500 °C (Zn/Sn = 1.01) and 550 °C (Zn/Sn = 0.98).

The Raman spectrum acquired with 514 nm excitation wave- length on the CZTS layer sulfurized at 550 °C (Zn/Sn = 0.98) is shown in Fig6. 12a. The main Raman modes were observed around 337 $cm^{-1}$and 287 $cm^{-1}$for A symmetry modes, while the E and B symmetry modes were centered at 253, 264, 272, 304, 316, 347, 355, 363 and 374 cm^{-1}. It is important to underline that with this sulfurization temperature and excitation wavelength the Raman mode that is attributed to the disordered kesterite around 331 cm^{-1} is much weaker comparing to other CZTS layers sulfurized at 500 °C (Figs6. 8 and 12). Resonant Raman excitation was also used in order to compare CZTS films formed at different sulfurization temperatures. The main A symmetry modes are around 287 $cm^{-1}$and 337 cm^{-1} for both the CZTS layers. The excitation wavelength of 785 nm increased the intensity of peaks around 303 cm^{-1}, 317 cm^{-1}, 366 $cm^{-1}$and 373 cm^{-1}. The position of the Lorentzian lineshapes shifted slightly at 300 cm^{-1} and at 306 cm^{-1} for the CZTS layers sulfurized at 500 °C and 550 °C, respectively (Fig6. 13). XRD patterns and Raman spectra results show relatively pure CZTS layers for the samples sulfurized at 500 _C with Zn/Sn ratio 1.34 and for that sulfurized at 550 °C with Zn/Sn ratio 0.98 (Figs. 6 and 11).These CZTS films showed not only a low fraction of secondary phases, but also a low intensity of XRD reflections around 16, 18, 37 and 38 2θ degree, which suggested the formation

of a well crystallized material (Figs6. 6 and 11). Raman Spectroscopy can be used to estimate the degree of order of well crystallized CZTS layers with small amount of minor phases. For this purpose, we compare the relative intensity of peaks at 337 cm–1 (main A Raman mode) I (337) and at 331 cm^{-1} (disorder related peak) I (331) (Figs6. 8d, 12a). The ratio I(337)/I(331) is 7.22 and 15.80 for CZTS layers formed at 500 °C and 550 °C, respectively, evidencing a higher order parameter for sulfurization at the higher temperature.

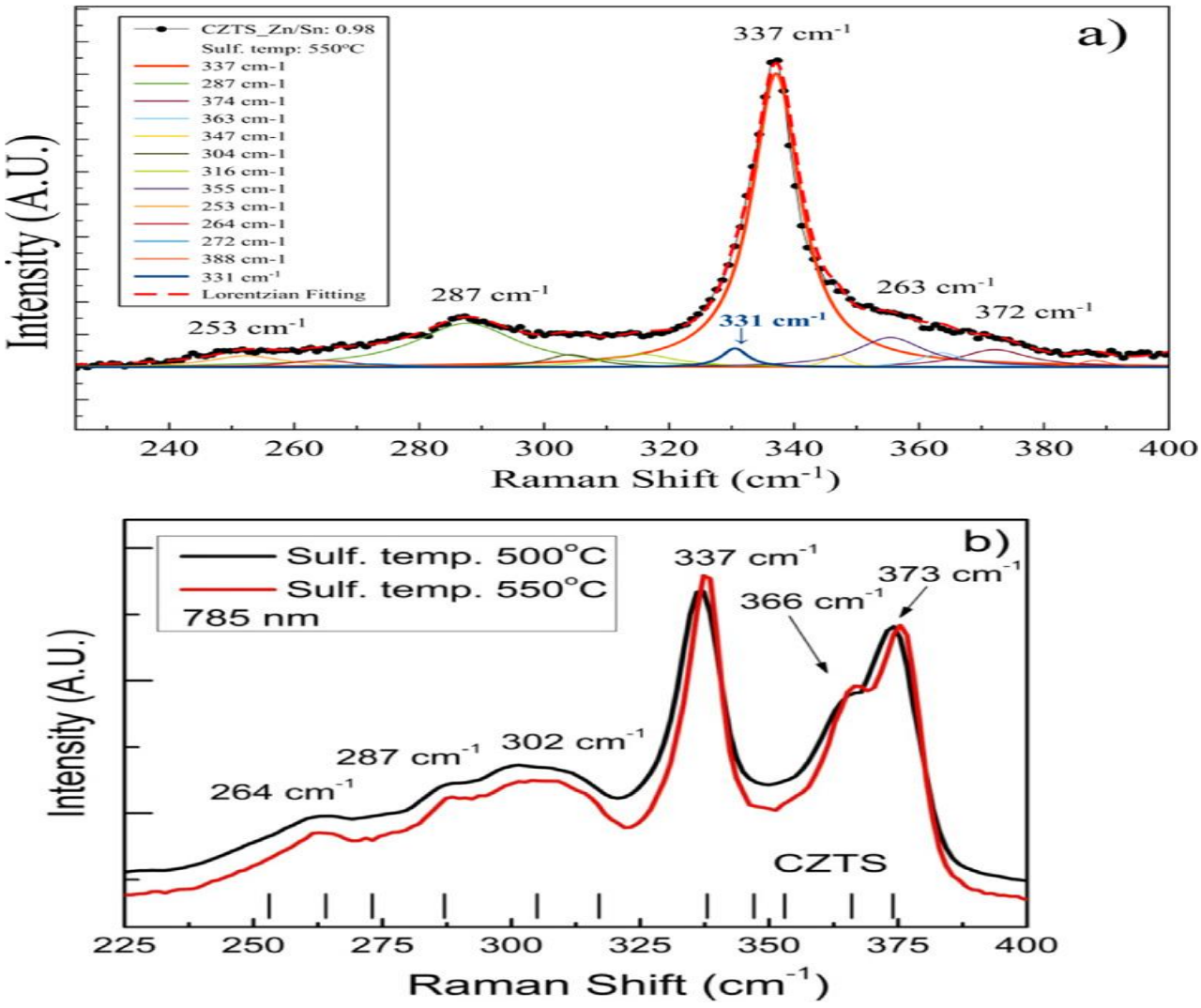

Fig6. 12. Raman Spectroscopy with a) 514 nm excitation wavelength and b) 785 nm for CZTS films sulfurized at 500 °C (Zn/Sn = 1.01) and 550 °C (Zn/Sn = 0.98).

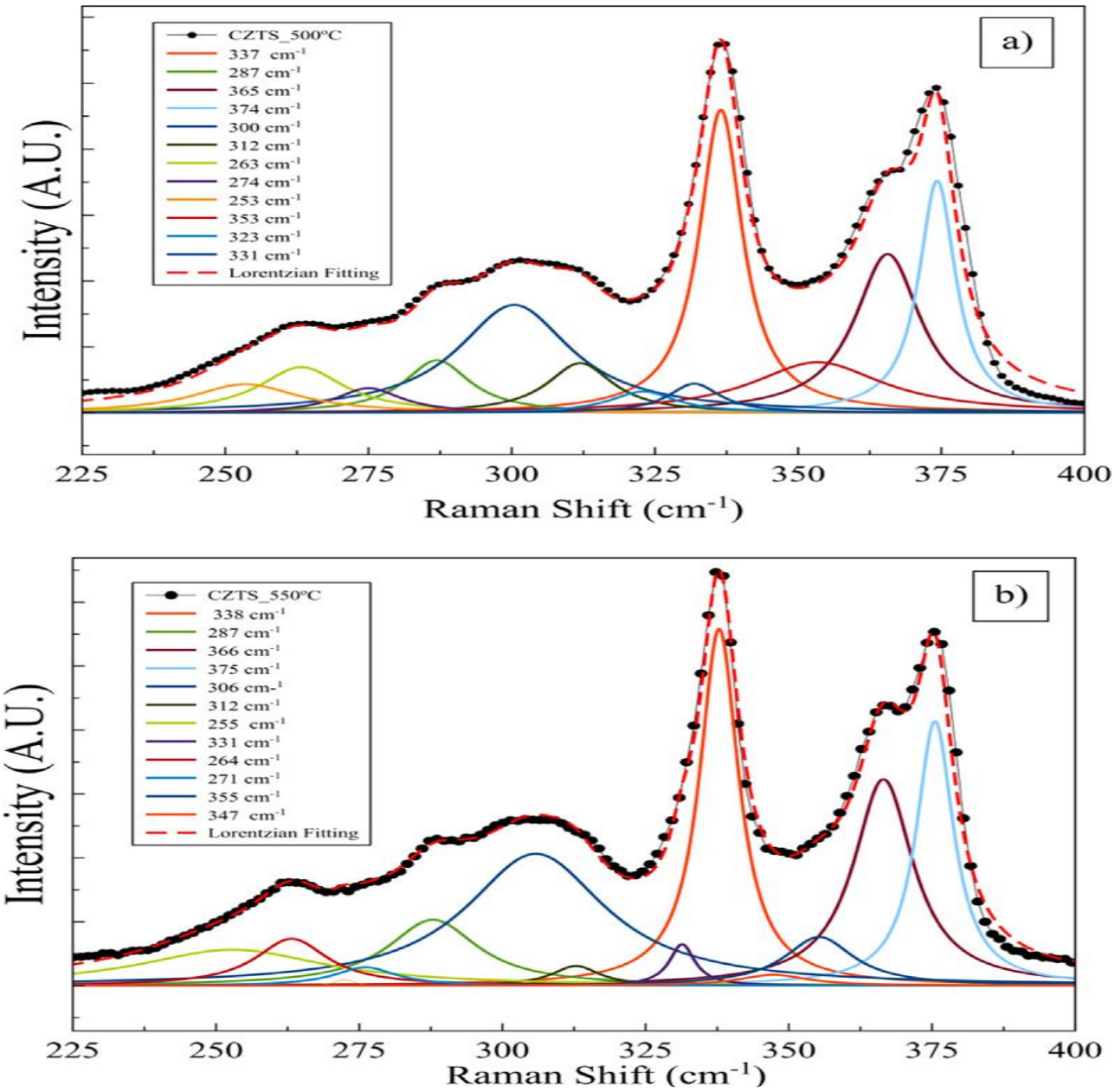

Fig6. 13. Lorentzian fitting for Raman spectra with excitation wavelength 785 nm for CZTS films sulfurized at a) 500 °C (Zn/Sn = 1.01) and b) 550 °C (Zn/Sn = 0.98).

This suggests that optimization of precursor composition and sulfuri-zation temperature not only improve the phase purity, but also the degree of order of the CZTS crystal. Fig6. 14. compares the photocurrent-potential curves for CZTS films sulfurized at 500°C and 550 °C. The PEC response increased with higher Zn/Sn ratio irrespective of sulfurization temperature. Close to stoichiometric CZTS layers after sulfurization at 550 °C show the highest PEC response of 0.99

mA/cm2 and the highest integral IPCE 3.54% compared to other samples. In the literature, the presence of some secondary phases like Cu-S is one of the major causes for the low open circuit voltage, which is limiting the solar cell performance. We observed an increase in PEC response for both sulfurization temperatures by increasing Zn/Sn ratio. XRD and Raman Spectroscopy results suggest that increasing Zn/Sn ratio and sulfurization temperature at 550 °C reduced the secondary phases and improved the relative order of the CZTS compared to 500 °C. Therefore, we attribute the increase in PEC response to the improvement of phase purity and the presence of a more ordered kesterite phase.

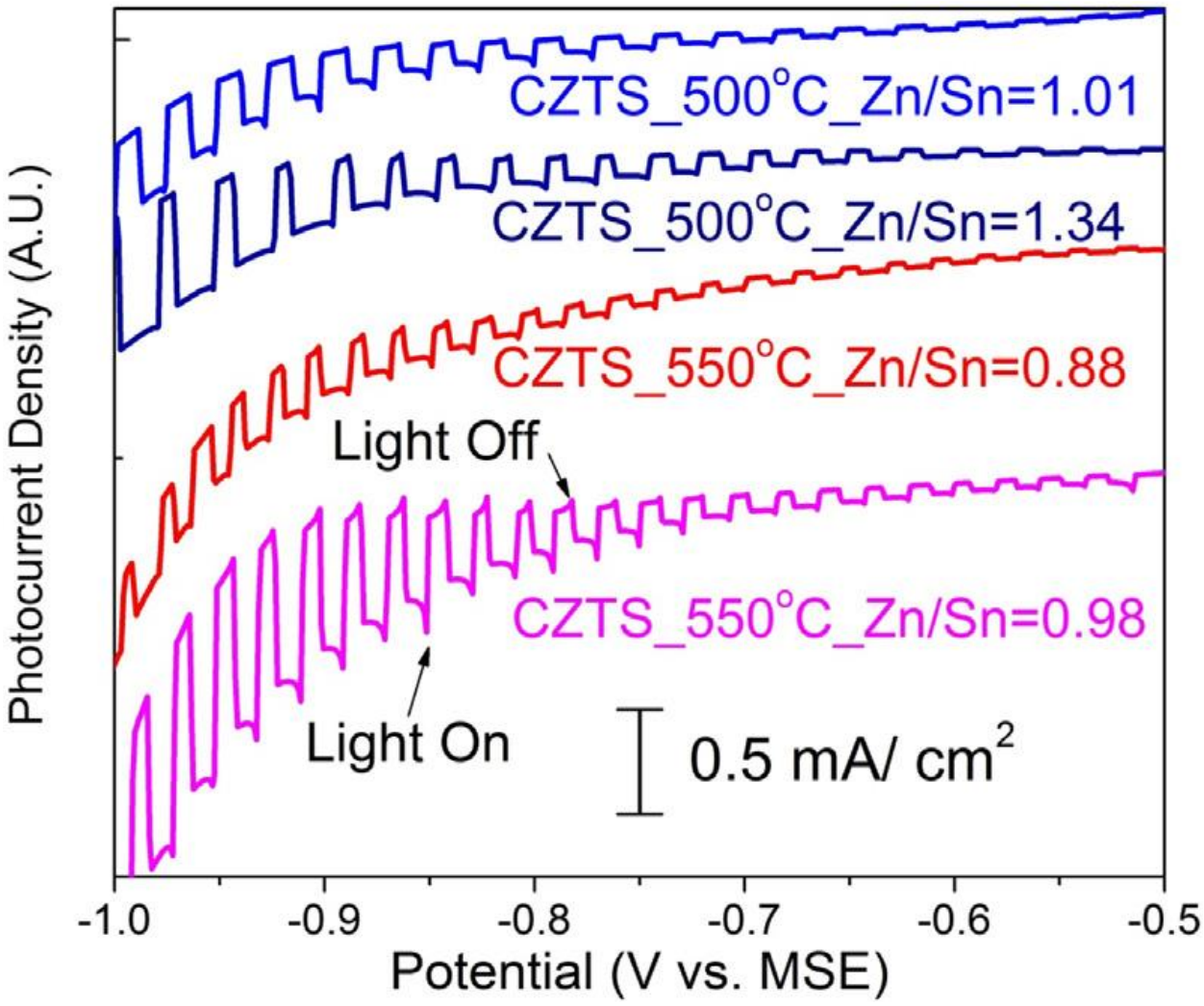

Fig6. 14. Photocurrent-potential curves for CZTS films sulfurized at 500 °C and 550 °C with different Zn/Sn ratio.

6.5 Conclusion

We have shown that the potential applied during electrodepo- sition of Cu-Zn-Sn can be used to keep the Cu fraction constant while controlling the Zn/Sn ratio within the suitable composition range for the formation of CZTS absorber layers. We also found that the initial composition and sulfurization temperature are influ-encing the loss of elements, hence the formation of secondary phases in CZTS layer. The use of Raman spectroscopy and XRD provided insight into the phase purity and the degree of Cu-Zn cation disorder in the CZTS layers with different Zn/Sn ratio and sulfurization temperature. The photoelectrochemical response of CZTS layers was improved by increasing Zn/Sn ratio for both sulfurization temperature, 500 °C and 550 °C, due to the formation of a lower fraction of secondary phases and improved crystal quality. We observed the highest photoelectrochemical response, 0.99 mA/cm2, for a CZTS layer with Zn/Sn ratio 0.98, after sulfurization at 550 °C. Qualitative Raman spectra investigation of kesterite thin films with minor secondary phases suggested that the enhanced response is mainly the result of improved order of the Cu-Zn cations and sulfurization at higher temperature. Further investigation is needed in order to understand the reason behind the increasing order of the Cu-Zn cations with increasing temperature.

References

[1] “Directions for the solar economy: PV roadmap 2020” Roland Berger Strategy Consultants. https://www.rolandberger.com/media/pdf/ Roland_Berger_Directions_for_Solar_Economy.

[2] Intergovernmental Panel on Climate Change, Fourth Assessment Report, 2015, Working Group III Report, Mitigation of Climate Change, 15.04.2015.

[3] Annual Renewable energy report (2013) of DOE.

[4] R. Noufi, K. Zweibel, High-efficiency CdTe and CIGS thin-film solar cells: Highlights and challenges, Conf. Rec. 2006 IEEE 4th World Conf. Photovolt. Energy Conversion, WCPEC-4. 1 (2007) 317–320, doi:http://dx.doi.org/ 10.1109/WCPEC.2006.279455.

[5] M. Redlinger, R. Eggert, M. Woodhouse, Evaluating the availability of gallium, indium, and tellurium from recycled photovoltaic modules, Sol. Energy Mater. Sol. Cells. 138 (2015) 58–71, doi:http://dx.doi.org/10.1016/j. solmat.2015.02.027.

[6] L.M. Peter, Towards sustainable photovoltaics: the search for new materials, Philos. Trans. R. Soc. A Math. Phys. Eng. Sci. 369 (2011) 1840–1856, doi:http:// dx.doi.org/10.1098/rsta.2010.0348.

[7] M.A. Green, K. Emery, Y. Hishikawa, W. Warta, E.D. Dunlop, Solar cell efficiency tables (Version 45), Prog. Photovoltaics Res. Appl. 23 (2015) 1–9, doi:http://dx. doi.org/10.1002/pip.2573.

[8] M. Grossberg, J. Krustok, K. Timmo, M. Altosaar, Radiative recombination in Cu2ZnSnSe4 monograins studied by photoluminescence spectroscopy, Thin Solid Films. 517 (2009) 2489–2492, doi:http://dx.doi.org/10.1016/j. tsf.2008.11.024.

[9] I. Repins, C. Beall, N. Vora, C. DeHart, D. Kuciauskas, P. Dippo, et al., Co-evaporated Cu2ZnSnSe4 films and devices, Sol. Energy Mater. Sol. Cells. 101 (2012) 154–159, doi:http://dx.doi.org/10.1016/j.solmat.2012.01.008.

[10] T.K. Todorov, J. Tang, S. Bag, O. Gunawan, T. Gokmen, Y. Zhu, et al., Beyond 11% Efficiency: Characteristics of State-of-the-Art Cu 2 ZnSn(S,Se) 4 Solar Cells, Adv. Energy Mater. 3 (2013) 34–38, doi:http://dx.doi.org/10.1002/ aenm.201200348.

[11] D.A.R. Barkhouse, O. Gunawan, T. Gokmen, T.K. Todorov, D.B. Mitzi, Device characteristics of a 10.1% hydrazine-processed Cu2ZnSn(Se,S)4 solar cell, Prog. Photovoltaics Res. Appl. 20 (2012) 6–11, doi:http://dx.doi.org/10.1002/pip.

[12] T.J. Huang, X. Yin, G. Qi, H. Gong, CZTS-based materials and interfaces and their effects on the performance of thin film solar cells, Phys. Status Solidi _ Rapid Res. Lett. 08 (2014) 735–762, doi:http://dx.doi.org/10.1002/pssr.201409219.

[13] W. Wang, M.T. Winkler, O. Gunawan, T. Gokmen, T.K. Todorov, Y. Zhu, et al., Device characteristics of CZTSSe thin-film solar cells with 12.6% efficiency, Adv. Energy Mater. 4 (2014) 1–5, doi:http://dx.doi.org/10.1002/aenm.201301465.

[14] J.J. Scragg, P.J. Dale, D. Colombara, L.M. Peter, Thermodynamic aspects of the synthesis of thin-film materials for solar cells, ChemPhysChem. 13 (2012) 3035–3046, doi:http://dx.doi.org/10.1002/cphc.201200067.

[15] J.J.S. Scragg, J.K. Larsen, M. Kumar, C. Persson, J. Sendler, S. Siebentritt, et al., Cu- Zn disorder and band gap fluctuations in Cu 2 ZnSn(S, Se) 4: Theoretical and experimental investigations, Phys. Status Solidi. (2015), doi:http://dx.doi.org/ 10.1002/pssb.201552530.

[16] D. Han, Y.Y. Sun, J. Bang, Y.Y. Zhang, H.B. Sun, X. Bin Li, et al., Deep electron traps and origin of p-type conductivity in the earth-abundant solar-cell material Cu2ZnSnS4, Phys. Rev. B _ Condens. Matter Mater. Phys. 87 (2013) 1–5, doi: http://dx.doi.org/10.1103/PhysRevB.87.155206.

[17] D. Colombara, a. Crossay, L. Vauche, S. Jaime, M. Arasimowicz, P.P. Grand, et al., Electrodeposition of kesterite thin films for photovoltaic applications: Quo vadis? Phys. Status Solidi Appl. Mater. Sci. 212 (2015) 88–102, doi:http://dx. doi.org/10.1002/pssa.201431364.

[18] R. Kondrotas, R. Jušk_ enas, a. Naujokaitis, a. Selskis, R. Giraitis, Z. Mockus, et al., Characterization of Cu2ZnSnSe4 solar cells prepared from electrochemically co-deposited Cu–Zn–Sn alloy, Sol. Energy Mater. Sol. Cells 132 (2015) 21–28, doi:http://dx.doi.org/10.1016/j.solmat.2014.08.010.

[19] M.F. de Carvalho, E.P. Barbano, I.a. Carlos, Electrodeposition of copper-tin-zinc ternary alloys from disodium ethylenediaminetetraacetate bath, Surf. Coatings Technol. 262 (2015) 111–122, doi:http://dx.doi.org/10.1016/j. surfcoat.2014.12.019.

[20] D.B. Mitzi, O. Gunawan, T.K. Todorov, K. Wang, S. Guha, The path towards a high-performance solution-processed kesterite solar cell, Sol. Energy Mater. Sol. Cells. 95 (2011) 1421–1436, doi:http://dx.doi.org/10.1016/j. solmat.2010.11.028.

[21] F. Jiang, S. Ikeda, T. Harada, M. Matsumura, Pure Sulfide Cu2ZnSnS4 thin film solar cells fabricated by preheating an electrodeposited metallic stack, Adv. Energy Mater. 4 (2014) 2–5, doi:http://dx.doi.org/10.1002/aenm.201301381.

[22] J. Tao, J. Liu, L. Chen, H. Cao, X. Meng, Y. Zhang, et al., 7.1% efficienct co– electroplated Cu2ZnSnS4 thin film solar cells with sputtered CdS buffer layers, Green Chem. (2015), doi:http://dx.doi.org/10.1039/C5GC02057C.

[23] A. Ennaoui, M. Lux-Steiner, a. Weber, D. Abou-Ras, I. Kötschau, H.-W. Schock, et al., Cu2ZnSnS4 thin film solar cells from electroplated precursors: Novel low- cost perspective, Thin Solid Films 517 (2009) 2511–2514, doi:http://dx.doi.org/ 10.1016/j.tsf.2008.11.061.

[24] C. Gougaud, D. Rai, S. Delbos, E. Chassaing, D. Lincot, Electrochemical Studies of One-Step Electrodeposition of Cu-Sn-Zn Layers from Aqueous Electrolytes for Photovoltaic Applications, J. Electrochem. Soc. 160 (2013) D485–D494, doi: http://dx.doi.org/10.1149/2.105310jes.

[25] M. Guo, X. Zhu, H. Li, Comparative study of Cu2ZnSnS4 thin film solar cells fabricated by direct current and pulse reverse co-electrodeposition, J. Alloys Compd. 657 (2015) 336–340, doi:http://dx.doi.org/10.1016/j. jallcom.2015.10.100.

[26] A. Alvarez, S. Exarhos, L. Mangolini, Tin disulfide segregation on CZTS films sulfurized at high pressure, Mater. Lett. 165 (2016) 41–44, doi:http://dx.doi. org/10.1016/j.matlet.2015.11.090.

[27] V. Piacente, S. Foglia, P. Scardala, Sublimation study of the tin sulphides SnS2, Sn2S3 and SnS, J. Alloys Compd. 177 (1991) 17–30, doi:http://dx.doi.org/ 10.1016/0925-8388(91)90053-X.

[28] R. Schurr, a. Hölzing, S. Jost, R. Hock, T. Vob, J. Schulze, et al., The crystallisation of Cu2ZnSnS4 thin film solar cell absorbers from co-electroplated Cu–Zn–Sn precursors, Thin Solid Films. 517 (2009) 2465–2468, doi:http://dx.doi.org/ 10.1016/j.tsf.2008.11.019.

[29] A. Weber, R. Mainz, H.W. Schock, On the Sn loss from thin films of the material system Cu-Zn-Sn-S in high vacuum, J. Appl. Phys.107 (2010) 1–6, doi:http://dx. doi.org/10.1063/1.3273495.

[30] M.C. Johnson, C. Wrasman, X. Zhang, M. Manno, C. Leighton, E.S. Aydil, Self-regulation of cu/sn ratio in the synthesis of Cu2ZnSnS4 films, Chem. Mater. 27 (2015) 2507–2514, doi:http://dx.doi.org/10.1021/acs.chemmater.5b00108.

[31] J.J. Scragg, T. Kubart, J.T. Wätjen, T. Ericson, M.K. Linnarsson, C. Platzer- Björkman, Effects of back contact instability on Cu2ZnSnS4 devices and processes, Chem. Mater. 25 (2013) 3162–3171, doi:http://dx.doi.org/10.1021/ cm4015223.

[32] Y.D. Gamburg, G. Zangari, Theory and practice of metal electrodeposition, Springer Science & Business Media, 2011.

[33] G.K. Dalapati, S.K. Batabyal, S. Masudy-Panah, Z. Su, A. Kushwaha, T.I. Wong, et al., Sputter grown sub-micrometer thick Cu2ZnSnS4 thin film for photovoltaic device application, Mater. Lett. 160 (2015) 45–50, doi:http://dx. doi.org/10.1016/j.matlet.2015.07.089.

[34] D. Colombara, P.J. Dale, G.P. Kissling, L.M. Peter, S. Tombolato, Photoelectrochemical Screening of Solar Cell Absorber Layers: Electron Transfer Kinetics and Surface Stabilization, J. Phys. Chem. C. (2016), doi:http:// dx.doi.org/10.1021/acs.jpcc.5b12531 acs.jpcc.5b12531.

[35] F. Oliva, S. Kretzschmar, D. Colombara, S. Tombolato, C.M. Ruiz, A. Redinger, et al., Optical methodology for process monitoring of chalcopyrite photovoltaic technologies: Application to low cost Cu(In,Ga)(S,Se)2 electrodeposition based processes, Sol. Energy Mater. Sol. Cells. (2016) 1–16, doi:http://dx.doi.org/10.1016/j.solmat.2015.12.036.

[36] M. Kumar, A. Dubey, N. Adhikari, S. Venkatesan, Q. Qiao, Strategic review of secondary phases, defects and defect-complexes in kesterite CZTS-Se solar cells, Energy Environ. Sci. 8 (2015) 3134–3159, doi:http://dx.doi.org/10.1039/ c5ee02153g.

[37] S. Chen, A. Walsh, X.-G. Gong, S.-H. Wei, Classification of lattice defects in the kesterite Cu2ZnSnS4 and Cu2ZnSnSe4 earth-abundant solar cell absorbers, Adv. Mater. 25 (2013) 1522–1539, doi:http://dx.doi.org/10.1002/adma.201203146.

[38] J.J. Scragg, T. Ericson, T. Kubart, M. Edoff, C. Platzer-Björkman, Chemical insights into the instability of Cu2ZnSnS4 films during annealing, Chem. Mater. 23 (2011) 4625–4633, doi:http://dx.doi.org/10.1021/cm202379s.

[39] P.A. Fernandes, P.M.P. Salom, Study of polycrystalline Cu 2 ZnSnS 4 films by Raman scattering, J. Alloys Compd. 509 (2011) 7600–7606, doi:http://dx.doi. org/10.1016/j.jallcom.2011.04.097.

[40] D. Dumcenco, Y.-S. Huang, The vibrational properties study of kesterite Cu2ZnSnS4 single crystals by using polarization dependent Raman spectroscopy, Opt. Mater. (Amst). 35 (2013) 419–425, doi:http://dx.doi.org/ 10.1016/j.optmat.2012.09.031.

[41] D.M. Berg, M. Arasimowicz, R. Djemour, L. Gütay, S. Siebentritt, S. Schorr, et al., Discrimination and detection limits of secondary phases in Cu2ZnSnS4 using X-ray diffraction and Raman spectroscopy, Thin Solid Films. 569 (2014) 113–123, doi:http://dx.doi.org/10.1016/j.tsf.2014.08.028.

[42] O. Brafman, S.S. Mitra, Raman effect in wurtzite- and zinc-blende-type ZnS single crystals, Phys. Rev. 171 (1968) 931.

[43] R. Caballero, E. Garcia-Llamas, J.M. Merino, I. Babichuk, V. Dzhagan, et al., Non-stoichiometry effect and disorder in Cu2ZnSnS4 thin films obtained by flash evaporation: Raman scattering investigation, Acta Mater. 65 (2014) 412–417, doi:http://dx.doi.org/10.1016/j.actamat.2013.11.010.

[44] M. Dimitrievska, A. Fairbrother, E. Saucedo, A. Pérez-Rodríguez, V. Izquierdo- Roca, Raman scattering crystalline assessment of polycrystalline Cu2ZnSnS4 thin films for sustainable photovoltaic technologies: Phonon confinement model, Acta Mater 70 (2014) 272–280, doi:http://dx.doi.org/10.1016/j. actamat.2014.02.035.

[45] M. Dimitrievska, A. Fairbrother, X. Fontane, T. Jawhari, V. Izquierdo-Roca, E. Saucedo, et al., Multiwavelength excitation Raman scattering study of polycrystalline kesterite Cu2ZnSnS4 thin films, Appl. Phys. Lett. 104 (2014) 4–9, doi:http://dx.doi.org/10.1063/1.4861593.

[46] N. Guijarro, M.S. Prevot, X.A. Jeanbourquin, X. Yu, K. Sivula, Autodecomposition Approach for the Low-Temperature Mesostructuring of Nanocrystal Semiconductor Electrodes, Chem. Mater. (2015), doi:http://dx.doi.org/ 10.1021/acs.chemmater.5b02894.

[47] Y. Zhang, S. Ouyang, Q. Yu, P. Li, J. Ye, Modulation of sulfur partial pressure in sulfurization to significantly improve the photoelectrochemical performance over the Cu2ZnSnS4 photocathode, Chem. Commun. 51 (2015) 14057–14059, doi:http://dx.doi.org/10.1039/c5cc04812e.

[48] L.M. Peter, Energetics and kinetics of light-driven oxygen evolution at semiconductor electrodes: the example of hematite, 550 (2013) 315–326, doi: 10.1007/s10008-012-1957-3.

[49] Chong Liu, Neil P. Dasgupta, P. Yang, Semiconductor Nanowires for Artificial Photosynthesis, Chem. Mater 26 (2014) 415–422, doi:http://dx.doi.org/ 10.1021/cm4023198.

[50] G. Altamura, J. Vidal, Impact of minor phases on the performances of CZTSSe thin film solar cells, Chem. Mater. (2016), doi:http://dx.doi.org/10.1021/acs. chemmater.6b00069 acs.chemmater.6b00069.